

## Modeling of caprock discontinuous fracturing during CO<sub>2</sub> injection into a deep brine aquifer

Peng-Zhi Pan <sup>a,b,\*</sup>, Jonny Rutqvist <sup>b</sup>, Xia-Ting Feng <sup>a</sup>, Fei Yan <sup>a</sup>

<sup>a</sup> State Key Laboratory of Geomechanics and Geotechnical Engineering, Institute of Rock and Soil Mechanics, Chinese Academy of Sciences, Wuhan 430071, China

<sup>b</sup> Lawrence Berkeley National Laboratory, MS 90-1116, Berkeley, CA 94720, USA



### ARTICLE INFO

#### Article history:

Received 6 March 2013

Received in revised form

14 September 2013

Accepted 12 October 2013

Available online 16 November 2013

#### Keywords:

Rock discontinuous cellular automaton

TOUGH2

CO<sub>2</sub> injection

Fracture propagation

Hydraulic fracturing

### ABSTRACT

In this paper, we present a discontinuous method for simulating coupled multiphase fluid flow and hydraulic fracturing, and apply this method to deep underground CO<sub>2</sub> injection. In this modeling approach, the individual physical processes involved in hydraulic fracturing are identified and addressed as separate modules: (1) a rock-discontinuous-cellular-automaton method for continuous-discontinuous geomechanical fracturing analysis, and (2) an integrated finite volume method for representing non-isothermal, multiphase fluid-flow processes. With this approach, the real fracture propagation path (straight or curved) induced by CO<sub>2</sub> injection can be modeled without the need for remeshing. We verify the method and the numerical model against analytical solutions for fracture opening and propagation. We then simulate CO<sub>2</sub> injection-induced fracturing within a brine aquifer, demonstrating the capability and applicability of our coupled numerical method for simulating fracturing processes driven by multiphase fluid flow. Our study focuses on the role of initial caprock damage in geologic carbon sequestration, and how natural fractures could impact caprock sealing integrity. We find that, given initial damage or fracturing in the lower part of the caprock, injection-induced pressure can diffuse into the fracture and potentially propagate upwards across the caprock, creating a new flow path by which CO<sub>2</sub> could migrate out of the intended storage aquifer. However, our modeling also shows that an injection pressure limited by minimum principal compressive stress (which might be estimated from leak-off or mini-frac tests) would be appropriate for safe injection with respect to maintaining caprock sealing integrity. Finally, our modeling also highlights the importance and usefulness of pressure and deformation monitoring—potentially effective techniques for early detection of deep fracture propagation breaking through a caprock layer.

© 2013 Elsevier Ltd. All rights reserved.

### 1. Introduction

Geologic carbon sequestration (GCS) achieved through deep underground injection of carbon dioxide (CO<sub>2</sub>) is being considered for sequestering CO<sub>2</sub> and thus reducing the emission of greenhouse gases to the atmosphere. However, any potential site for GCS must be considered carefully. Geomechanics plays an important role in the performance assessment of such a CO<sub>2</sub> injection site, including assessment of caprock sealing performance, ground-surface deformations, and the potential for fault reactivation and induced seismicity (Rutqvist, 2012). Given that CO<sub>2</sub> is buoyant relative to water, any targeted CO<sub>2</sub> injection reservoir should be

overlain by low-permeability caprock that can sufficiently limit upward buoyancy-driven flow of the injected CO<sub>2</sub>. A geomechanical analysis of GCS requires coupled fluid flow and geomechanical models with appropriate capabilities for the problem at hand.

In recent years, a number of coupled fluid flow and geomechanical numerical models have emerged as suitable for analyzing various geomechanical issues associated with GCS (Rutqvist, 2012). Desirable capabilities for such a numerical simulator include the capturing of nonisothermal multiphase flow and transport for supercritical CO<sub>2</sub> and brine coupled with geomechanical processes. Examples of numerical simulators applied to study these geomechanical aspects of GCS include TOUGH-FLAC (Rutqvist et al., 2002; Rutqvist, 2011), FEMH (Bower and Zywoloski, 1997; Deng et al., 2011), OpenGeoSys (Wang and Kolditz, 2007; Goerke et al., 2011), CODE-BRIGHT (Olivella et al., 1994; Vilarrasa et al., 2010), ECLIPSE-VISAGE (Ouellet et al., 2011), STARS (CMG, 2003; Bissell et al., 2011), NUFT-SYNEF (Morris et al., 2011), DYNAFLOW (Preisig and Prévost, 2011), as well as other simulators in which multiphase flow codes

\* Corresponding author at: State Key Laboratory of Geomechanics and Geotechnical Engineering, Institute of Rock and Soil Mechanics, Chinese Academy of Sciences, Wuhan 430071, China. Tel.: +86 27 87198805; fax: +86 27 87197386.

E-mail address: [pzpan@whrsm.ac.cn](mailto:pzpan@whrsm.ac.cn) (P.-Z. Pan).

(such as TOUGH2, ECLIPSE, and GEM) have been linked with geomechanical codes (Ferronato et al., 2010; Rohmer and Seyed, 2010; Tran et al., 2010).

The aforementioned numerical simulators have been applied for modeling large-scale geomechanical processes associated with GCS, including stress changes, ground-surface uplift, and fault reactivation. In this paper, we develop and apply a model for analyzing discrete fracture propagation related to the potential for hydraulic fracturing of caprock, as a result of high pressurization caused by CO<sub>2</sub> injection. This is a complex problem involving both large-scale coupled fluid-flow, geomechanical processes and small-scale processes occurring at the tip of a crack or several cracks.

Moreover, the problem is also complicated by the existence of heterogeneities such as natural fractures. For example, if there were initial fracturing within the caprock connected to a CO<sub>2</sub> storage aquifer, the fluid pressure could diffuse into the fracture, and (if the pressure were sufficiently high) the fracture could propagate. Fracturing through caprock could create an upward migration path for stored CO<sub>2</sub> that could significantly reduce the seal integrity of the caprock. The coupled multiphase flow and geomechanical processes associated with such fracturing could be further complicated by buoyancy forces, as brine is replaced with a less-dense supercritical CO<sub>2</sub>. For studying such processes, it is desirable to have a numerical modeling tool that could simulate both large-scale multiphase fluid flow and geomechanical processes, and discrete fracturing processes, driven by multiphase fluid flow such as supercritical CO<sub>2</sub> or brine.

Numerous numerical models for hydraulic fracturing developed over recent years have been used in reservoir engineering applications. These applications include the exploration and development of hydrocarbons or geothermal reservoirs (Murphy et al., 1981; Mandl and Harkness, 1987; Legarth et al., 2005), estimation of *in situ* stress in rock masses (Haimson and Fairhurst, 1969; Bredehoeft et al., 1976), and deep underground injection disposal of hazardous liquid and solid wastes (Dusseault et al., 1996). Early work of this sort includes Shaffer et al. (1984), who developed and applied the FFFLAP simulator for modeling of fluid-driven fracture propagation in rock masses with pre-existing discontinuities, and Boone and Ingraffea (1990), who developed and applied software for high-performance computing and visualization of hydraulic fracture propagation in poroelastic media.

More recently, a number of alternative techniques and numerical methods have been developed and applied to hydraulic fracturing (Carter et al., 2000; Peirce and Detournay, 2008, 2009; Ji et al., 2009; Lecampion, 2009; Ren et al., 2009; Kovalyshen, 2010; Segura and Carol, 2010; Shin and Santamarina, 2010; Xu and Wong, 2010; Fareo and Mason, 2011; Sarris and Papanastasiou, 2011; Zhang et al., 2011; Carrier and Granet, 2012; Fu et al., 2012). These alternative approaches include using an implicit level set method (Peirce and Detournay, 2008), a Eulerian moving-front algorithm with weak-form tip asymptotics (Peirce and Detournay, 2009), a finite element method (Xu and Wong, 2010), an extended finite element method (Ren et al., 2009), a zero-thickness finite element method (Segura and Carol, 2010), and a node-splitting method (Fu et al., 2012).

The many different modeling approaches investigated over the years attest to the fact that numerically simulating the propagation of hydraulic fractures is widely known to be a difficult problem, with nonlinear and nonlocal properties enhanced by the presence of a moving internal boundary. For example, continuum-framework-based numerical methods (e.g., FEM) require that the mesh conform precisely to the fracture geometry at all times, which means that computationally expensive remeshing algorithms must be used to track the propagation of a fracture (Hillerborg et al., 1976). The alternative boundary-integral-equation, or displacement-discontinuity methods, cannot

be efficiently used to solve coupled poroelasticity equations relating the fluid pressure to the fracture opening (Lecampion, 2009). To avoid the remeshing step in fracture modeling, investigators have proposed several techniques (e.g., moving mesh techniques, XFEM—Rashid, 1998; Belytschko and Black, 1999; Moës et al., 1999; Oliver et al., 2002; Richardson et al., 2011). However, the coupling of flow and geomechanics by XFEM is still not a proven or tested method.

In this paper, we present a numerical model for multiphase flow-driven fracture propagation, that we then apply to the study of caprock fracture propagation associated with geologic CO<sub>2</sub> storage. This numerical model aims to effectively model coupled multiphase flow and geomechanical processes in heterogeneous rock, including explicit modeling of discontinuities such as fractures and faults, as well as propagation of fractures. We utilize recent developments related to the rock-discontinuous-cellular-automaton (RDCA) modeling approach for failure processes in strongly heterogeneous rock, without the need for remeshing (Pan et al., 2012). In RDCA, a discontinuity and the crack tip is represented by specially designed mathematical shape functions to model the displacement discontinuity and high-gradient stress field near the crack tip. By doing so, we can cut the element by a crack at any position, and a fracture can intersect elements and propagate through elements in an arbitrary direction, without the need for remeshing (except that additional subelements are added along the crack propagation path).

Here, we extend the RDCA approach to multiphase fluid-driven failure processes, including fracture propagation. This is accomplished by linking RDCA with TOUGH2, a finite volume code that simulates nonisothermal, multiphase flow (Pruess et al., 1999) in reservoirs. In this case, geometrically equivalent element grids are used in both RDCA and TOUGH2, and the two codes are sequentially coupled (Pan et al., 2013). When fractures propagate through the mesh in the RDCA, the permeability of the finite volume elements in the TOUGH2 are updated to implicitly represent the increased fracture permeability. TOUGH2 continuum representation, while an approximation, still provides a pragmatic modeling approach for representing multiphase flow and fracture propagation in a complex heterogeneous rock mass without the need for remeshing. The approximation in the TOUGH2 implicit continuum representation of the discrete fracture becomes more accurate with finer mesh discretization, which is needed anyway in the RDCA for accurate modeling of the fracturing process. Within this model, we can invoke two different criteria for fracturing, a *toughness-based criterion* or a *modified Mohr–Coulomb criterion*. The toughness-based criterion includes mixed Mode I (extension) and Mode II (shear) fracture propagation, whereas the Mohr–Coulomb criterion is modified with a tension cut-off, enabling modeling of both shear and tensile failure.

In this paper, we first present the governing equations for thermo-poroelasticity in porous media and rock discontinuities, including criteria for propagation of fractures. We then describe in more detail how fractures are discretized into the model, introducing the TOUGH-RDCA simulator (Pan et al., 2013), as well as model verifications for simulating fracture opening and propagation. Thereafter, we present a number of TOUGH-RDCA simulations related to CO<sub>2</sub> injection-induced fracturing of caprock, where we study fracture propagation and CO<sub>2</sub> migration. We end with a discussion of the maximum sustainable injection pressure and the potential for early detection of deep fracture propagation and CO<sub>2</sub> migration across caprock layers. Note that the current version of RDCA is limited to 2D analysis. Its capabilities include (1) single and multiple (e.g., fracture-intersection) fracturing analyses; (2) linear elastic analysis, and (3) elasto-plastic analysis. Current work is limited to linear elastic behavior and single fracturing under multiphase fluid flow conditions. (Multiple fracturing and elasto-plastic analyses will be the subject of future work.) TOUGH2 offers

the option of nonisothermal, multiphase fluid functionality, but in this work, we switch off the thermal option, considering isothermal processes exclusively.

## 2. Governing equations

We present in this section the governing equations for porous media thermo-poro-elasticity (Pruess et al., 1999), discontinuous mechanical and hydraulic behavior, and fracture propagation.

### 2.1. Porous media thermo-poro-elasticity

In this study, the fluid and solid skeletons are viewed as overlapping continua. The governing equations for heat and fluid flow and mechanics are obtained from energy, mass, and linear-momentum balances, respectively. For multiphase fluid flow, the mass-conservation equation is expressed as:

$$\frac{dm_j}{dt} + \text{Div}(\omega_j) = q_j \quad (1)$$

where the subscript  $J$  denotes a particular fluid phase.  $m_j$  is fluid mass,  $q_j$  is a source term, and  $\omega_j$  is the mass flux of fluid phase  $J$  relative to the motion of the solid skeleton. The accumulation term,  $dm_j/dt$ , also describes the time variation in fluid mass relative to the motion of the solid skeleton.  $\text{Div}(.)$  is a divergence operator.

The volumetric flux of phase  $J$ ,  $\mathbf{v}_J = (\omega/\rho)_J$ , is given by Darcy's law as

$$\mathbf{v}_J = -\frac{\mathbf{k}_{p,JK}}{J} (\mathbf{Grad} \mathbf{p}_K - \rho_K \mathbf{g}) \quad (2)$$

where  $\mathbf{k}_{p,JK}$  is the effective-permeability tensor (for fluid phases,  $J$  and  $K$ ).  $J$  and  $\rho_J$  denote the viscosity and density at the current state for fluid phase  $J$ , respectively.  $\mathbf{Grad}(\bullet)$  is a gradient operator. Double indices here indicate summation. In reservoir simulation,  $\mathbf{k}_{p,JK}$  is split into an absolute permeability  $k_p$  and a relative permeability  $k_{JK}^r$ , which is expressed as  $\mathbf{k}_{p,JK} = k_p k_{JK}^r$ , where  $k_{JK}^r = 0$  if  $J \neq K$ .  $\mathbf{g}$  is the gravity vector.

The governing equation for heat flow comes from energy balance, which is written as

$$\frac{dm^\theta}{dt} + \text{Div}(f^\theta) = q^\theta \quad (3)$$

where the superscript  $\theta$  indicates the heat component.  $m^\theta$ ,  $f^\theta$  and  $q^\theta$  are heat and its flux and source terms, respectively. Heat  $m^\theta$  is expressed as

$$m^\theta = (1 - \phi) \rho_R C_R T + \phi (S_\rho)_J e_J \quad (4)$$

where  $\rho_R$  and  $C_R$  are the density and heat capacity of the porous medium.  $S_J$  is saturation for fluid phase  $J$ ,  $T$  is temperature,  $e_J$  is the specific internal energy of phase  $J$ , and  $\phi$  is the true porosity, defined as the ratio of the pore volume to the bulk volume in the deformed configuration. The heat flux  $f^\theta$  driven by conduction and convection is expressed as

$$f^\theta = -((1 - \phi) \mathbf{K}_R + \phi S_J \mathbf{K}_J) \mathbf{Grad} T + h_J \omega_J \quad (5)$$

where  $\mathbf{K}_R$  and  $\mathbf{K}_J$  are the thermal conductivity tensors of the porous medium and fluid phase  $J$ , respectively.  $h_J$  is the specific enthalpy for phase  $J$ .

The governing equation for mechanics is given by the quasi-static assumption as

$$\text{Div} \sigma + \rho_b \mathbf{g} = 0 \quad (6)$$

where  $\sigma$  is the Cauchy total stress tensor.  $\rho_b (= \phi S_J \rho_J + (1 - \phi) \rho_R)$  is the bulk density. Based on the small deformation assumption, the

strain tensor is the symmetric gradient of the displacement vector and is expressed as

$$\boldsymbol{\varepsilon} = \frac{1}{2} (\mathbf{Grad} \mathbf{u} + \mathbf{Grad}^T \mathbf{u}) \quad (7)$$

where  $\boldsymbol{\varepsilon}$  and  $\mathbf{u}$  are the strain and displacement vectors, respectively. Tension and extensile strain are positive in this study.

The constitutive relations within an isotropic linear thermo-poroelastic medium can be expressed in terms of the effective stress  $\sigma'_{ij}$ , strain  $\varepsilon_{ij}$ , and temperature change  $\Delta T$  as (Pan et al., 2009),

$$\sigma'_{ij} = 2G \left( \varepsilon_{ij} + \delta_{ij} \frac{\nu}{1 - 2\nu} \varepsilon_{kk} \right) - K' \alpha_T \Delta T \delta_{ij} \quad (8)$$

where  $\sigma'_{ij} = \sigma_{ij} + \xi \bar{p} \delta_{ij}$  and  $\sigma_{ij}$  is the total stress (positive for tension),  $\delta_{ij}$  is the Kronecker delta,  $\xi (\leq 1)$  is Biot coefficient.  $\alpha_T$  is the linear expansion coefficient of temperature.  $K'$  is bulk modulus of rock mass.  $\bar{p}$  is average pore pressure defined as

$$\bar{p} = S_I p_I + (1 - S_I) p_g \quad (9)$$

For rock fractures, the fluid pressure is applied within the fractures normal to the fracture surfaces. If we neglect the shear stress induced by a flowing fluid on the fracture surface, the effective stress is expressed as

$$\sigma'_n = \sigma_n + \xi \bar{p} \quad (10)$$

Isotropic hydromechanical rock properties are represented by porosity-mean stress and permeability-porosity relationships. In this study, the porosity,  $\phi$ , is related to the mean effective stress as (Rutqvist and Tsang, 2002)

$$\phi = (\phi_0 - \phi_r) \exp(\alpha \sigma'_M) + \phi_r \quad (11)$$

where  $\phi_0$  is porosity at zero stress,  $\phi_r$  is residual porosity at high stress, and the exponent  $\alpha$  should be experimentally determined, while the mean effective stress is defined from the stress components as

$$\sigma'_M = \frac{1}{3} (\sigma'_x + \sigma'_y + \sigma'_z) \quad (12)$$

For rock matrix, the permeability is correlated to the porosity according to the following exponential function (Rutqvist and Tsang, 2002):

$$k = k_0 \exp \left[ c \left( \frac{\phi}{\phi_0 - 1} \right) \right] \quad (13)$$

where  $k_0$  is the zero stress permeability, and the exponent  $c$  is experimentally determined.

In this paper, isotropic mechanical relationships are used for simplicity, although shale in a caprock may be anisotropic, and such mechanical and hydraulic anisotropy might have some effect on the fracture propagation process. For sandstone formations, isotropic rock is a valid assumption, although anisotropy is possible, especially in the case of a fractured sandstone reservoir. The parameters  $\alpha$  and  $c$ , in defining the stress-versus-permeability function, are also taken to be the same for all layers, even though the permeability and porosity values  $k_0$ ,  $\phi_0$ , and  $\phi_r$  are (as expected) substantially different in sandstone and shale layers. With the selected parameters, a one-order-of-magnitude change in permeability is possible as a result of changes in mean stress, along with fluid pressurization. This is in agreement with matched laboratory data in Rutqvist and Tsang (2002) regarding sandstone, whereas stronger changes of up to 2 or 3 orders of magnitude can be possible in certain shales, such as in the Pierre shale (Rutqvist and Stephansson, 2003). However, in our simulations, these changes in permeability are relatively insignificant in comparison with changes occurring as a result of fracturing, which is the focus of this study.

## 2.2. Rock discontinuities

Rock discontinuities such as fractures and faults are modeled explicitly as discrete cracks or fractures having two rough surfaces that may be in contact locally, with fluid-filled voids between the areas of contact. Fluids can flow along the fractures depending on their aperture, which in turn depends on effective stress within the fracture, and could also change as a result of shear-induced dilation of the rough fracture surfaces.

The basic contact behavior of discontinuities is described by the shear stiffness  $K_s$  the normal stiffness  $K_n$ , cohesion  $c$ , and the coefficient of friction  $\mu$ . In modeling, the mechanical modes of discontinuities are associated with different mechanical processes, such as opening and shearing with stick and slip.

The stick mode, i.e.,  $t_s < 0$  and  $t_n < c + |t_n|$ , depends on  $K_s$  and  $K_n$  at a node inside each one-dimensional discontinuity element by

$$t_s = K_s D_s, \quad t_n = K_n D_n \quad (14)$$

where  $t_s$  and  $t_n$  are shear and normal tractions, respectively; and  $D_s$  and  $D_n$  are the shear and normal displacement on the crack surface, respectively.

If  $D_n > 0$ , the crack is open. In this case, the shear and normal tractions vanish, i.e.,

$$t_s = 0, \quad t_n = 0 \quad (15)$$

If  $t_n < 0$  and  $|t_s| \geq c + |t_n|\mu$ , a relatively tangential slip occurs. This behavior can be expressed as

$$t_s = \text{sign}(D_s)(c + |t_n|\mu) \quad t_n = K_n D_n \quad (16)$$

The permeability of the continuum element intersected by a fracture is calculated as

$$k = k_m + k_f \quad (17)$$

where  $k_m$  is the rock-matrix permeability and  $k_f$  is the fracture permeability. The fracture permeability is calculated by the cubic relation between aperture and fracture flow according to the following approximate equation:

$$k_f = \frac{h^3}{12b} \quad (18)$$

where  $b$  is estimated as the mean size of the element taken as the square root of the element area, and  $h$  is the hydraulic conducting aperture. Eqs. (17) and (18) provide a simplification related to the estimation of  $b$ , which we consider reasonably accurate, because the resulting permeability is strongly dependent on  $h$  through its cubic dependency. However, at the same time, we acknowledge that this is a simplified pragmatic approach; a possibly more precise and elaborate approach not considered in the present study would be to add a special TOUGH2 element along the trace of the propagating fracture.

## 2.3. Fracture propagation

Fractures can propagate in the case of high internal fluid pressure or other stress conditions that lead to stresses exceeding the criterion for fracture propagation. As mentioned above, in this study we consider two sets of criteria for describing the fracturing behavior, a toughness-based fracturing criterion and a modified Mohr–Coulomb criterion with tension cut-off.

### 2.3.1. Toughness-based fracturing criterion

Toughness-based fracturing conditions with stress intensity factor have been used widely in engineering (Pan et al., 2012). In this case, to judge whether a crack will propagate, linear-elastic-fracture mechanics and the stress intensity factor (SIF) (Knott, 1973; Broek, 1982; Kanninen and Popelar, 1985; Atkinson, 1987)

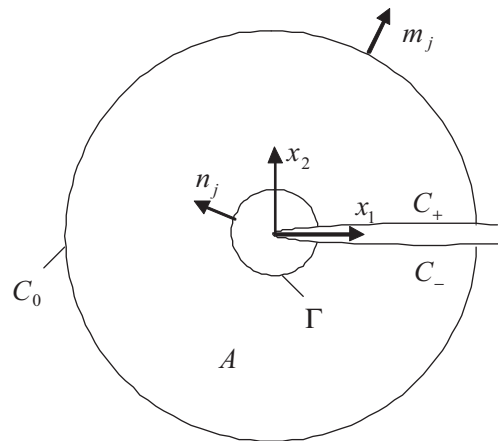


**Fig. 1.** Representation of interaction integral at crack tip.

concept are applied. For a two-dimensional problem, the stress intensity factor for mixed mode failure is

$$J = \frac{K_I^2}{E^*} + \frac{K_{II}^2}{E^*} \quad (19)$$

For plane stress,  $E^* = E$ , whereas for plane strain,  $E^* = E/1 - \nu^2$ .

Consider two equilibrium states of the body, i.e., State 1 and State 2. State 1 is the actual state of the body and State 2 is an auxiliary state. Field variables associated with the two states are denoted with superscripts 1 and 2. Superposition of the two equilibrium states leads to another equilibrium state denoted by an integral  $J^{(1+2)}$ .

$$J^{(1+2)} = \int_{\Gamma} \left[ \frac{1}{2} (\sigma_{ij}^{(1)} + \sigma_{ij}^{(2)}) (\varepsilon_{ij}^{(1)} + \varepsilon_{ij}^{(2)}) \delta_{ij} - (\sigma_{ij}^{(1)} + \sigma_{ij}^{(2)}) \frac{\partial(u_i^{(1)} + u_i^{(2)})}{\partial x_j} \right] n_j d\Gamma \quad (20)$$

We can write a simplified form of the above equation:

$$J^{(1+2)} = J^{(1)} + J^{(2)} + M^{(1,2)} \quad (21)$$

Assuming that the crack surface near the crack tip is straight and is within the integral boundary  $C_0$  shown in Fig. 1, the interaction integral item  $M^{(1,2)}$  can be expressed as

$$M^{(1,2)} = \int_C \left[ \sigma_{ij}^{(1)} \frac{\partial u_i^{(2)}}{\partial x_1} + \sigma_{ij}^{(2)} \frac{\partial u_i^{(1)}}{\partial x_1} - W^{(1,2)} \delta_{ij} \right] q m_j dC - \int_{C_+ + C_-} \left[ \sigma_{i2}^{(1)} \frac{\partial u_i^{(2)}}{\partial x_1} + \sigma_{i2}^{(2)} \frac{\partial u_i^{(1)}}{\partial x_1} - W^{(1,2)} \delta_{ij} \right] q m_j dC \quad (22)$$

where  $C = \Gamma \cup C_+ \cup C_- \cup C_0$ ,  $m_j$  is the outward normal vector to the domain boundary and  $q$  is a weight function.

The second term for the right-hand side in Eq. (22) considers the effect of fluid pressure on the crack surface.

The failure of a rock mass can be modeled using mixed-mode cracking. Several criteria—such as the maximum circumferential stress criterion, maximum tangential stress criterion, and minimum strain energy criterion—are often used to determine cracking conditions (Mohammadi, 2008). Specifically, the criterion provides the amount and direction of crack advancement. Take

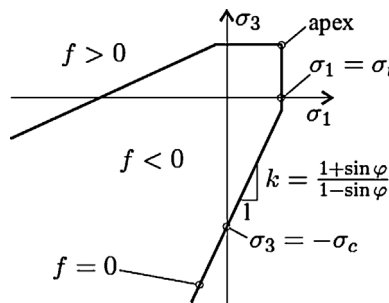


Fig. 2. Mohr–Coulomb criterion with tension cut-off.

the maximum circumferential stress criterion as an example: an explicit solution for the direction of crack propagation would be:

$$\theta_c = 2 \tan^{-1} \left[ \frac{1}{4} \left( \frac{K_I}{K_{II}} - \text{sign}(K_{II}) \sqrt{8 + \left( \frac{K_I}{K_{II}} \right)^2} \right) \right] \quad (23)$$

where angle  $\theta_c$  is defined with respect to a local polar coordinate system, with its origin at the crack tip and its alignment along the direction of the existing crack. Once the crack growth orientation is determined, a propagation increment is added to the existing crack, and the analysis procedure is repeated. The stress intensity factors  $K_I$  and  $K_{II}$  are calculated using the domain form of the interaction integral, which can be seen in the work by [Mohammadi \(2008\)](#).

### 2.3.2. Mohr–Coulomb criterion with tension cut-off

The Mohr–Coulomb criterion in combination with a tensile criterion is frequently used in both rock mechanics and rock engineering. Furthermore, the toughness-based fracturing criterion is typically employed in small-scale fracture propagation ([Adachi et al., 2007](#)), whereas for simulations of large-scale geological systems (e.g., CO<sub>2</sub> injection into a brine geological formation), the Mohr–Coulomb criterion with tension cut-off may be more practical. The numerical model developed in this study has both options, though in this paper we employ the Mohr–Coulomb criterion with tension cut-off to determine the condition of fracturing propagation (Fig. 2).

The Mohr–Coulomb criterion uses the well-known parameters of internal friction angle,  $\varphi$ , and cohesion,  $C$ , and may be expressed as

$$f_{MC} = k\sigma_1 - \sigma_3 - \sigma_c = 0 \quad \text{with} \quad k = \frac{1 + \sin \varphi}{1 - \sin \varphi} \quad \text{and} \quad \sigma_c = 2C\sqrt{k} \quad (24)$$

where  $\sigma_1$  and  $\sigma_3$  are the maximum and minimum principal stresses, with positive values signifying tensile stress.

Experimental results have shown that the Mohr–Coulomb model frequently overpredicts the tensile strength of a material ([Niels and Matti, 2005](#)). This discrepancy can be avoided by introducing the Rankine or “tension cut-off” criterion,

$$f_R = \sigma_1 - \sigma_t = 0 \quad (25)$$

where  $\sigma_t$  is the “tension cut-off” value, the highest tensile stress allowed in the material. The combination of these criteria is usually referred to as the Modified Mohr–Coulomb Criterion ([Niels and Matti, 2005](#)). The propagation direction is also determined by the criterion. For tensile fracturing, the propagation occurs in the plane is normal to the minimum compressive principal stress.

For shear fracturing, the fracturing direction is determined by

$$\alpha_s = \frac{90^\circ + \varphi}{2} \quad (26)$$

where  $\varphi$  is friction angle.

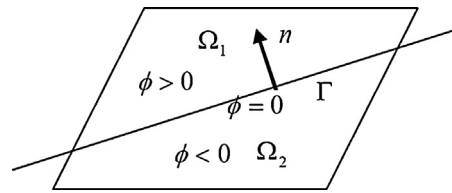


Fig. 3. Representation of level set function.

### 3. Discretization

To solve the governing equations, time and space are discretized. We employ the backward Euler method for time discretization. Since this study focuses on sequential coupling between fluid flow and mechanics, different space discretizations are used. For fluid and heat flow, the finite volume method is used where pressure and temperature are located at the cell center ([Pruess and Spycher, 2007](#)). For mechanical processes, a nodal-based space discretization method is used, in which the displacement vector is located at element vertices. A shape function is used to interpolate the displacement field within each element, based on the displacement at element vertices. Unlike the continuum method, we introduce special shape functions, i.e., the Heaviside function (step function) to simulate the crack surface and the asymptotic crack-tip displacement field function to approximate a discontinuous displacement field.

In order to consider the cracking behavior, we use an approximation of the discontinuous displacement field expressed as ([Moës et al., 1999](#)),

$$\begin{aligned} u^h(x) = & \sum_{i \in N} N_i(x) u_i + \sum_{j \in N^{dis}} N_j(x) H(\xi(x)) a_j \\ & + \sum_{k \in N^{asy1}} N_k(x) \left( \sum_{\alpha=1}^{mf} F_\alpha^1(x) b_k^{\alpha 1} \right) \\ & + \sum_{k \in N^{asy2}} N_k(x) \left( \sum_{\alpha=1}^{mf} F_\alpha^2(x) b_k^{\alpha 2} \right) \end{aligned} \quad (27)$$

where  $N$  represents the total nodal number of elements;  $N^{dis}$  is the total nodal number on an element intersected completely by a crack;  $N^{asy1}$  and  $N^{asy2}$  are the sets of nodes associated with crack tips 1 and 2 in their influence domain, respectively;  $N_i$ ,  $N_j$ , and  $N_k$  are the shape functions of the associated node;  $u_i$  is the nodal displacement (standard degrees of freedom); and  $a_j$ ,  $b_k^1$  and  $b_k^2$  are the vectors of the additional degrees of nodal freedom for modeling crack faces and the two crack tips, respectively.  $\xi$  is the value of the level set function, and  $H(\xi)$  is a Heaviside enrichment function that models the strong discontinuity caused by the crack.  $F_\alpha^1(x)$  and  $F_\alpha^2(x)$  represent the crack-tip asymptotic displacement field functions, which reflect the stress singularity at the crack tip.

We use the level-set method to track moving interfaces ([Osher and Sethian, 1988](#)). The level-set function  $\phi(x)$  is defined as (Fig. 3)

$$\phi(x) = \begin{cases} > 0 & x \in \Omega_1 \\ = 0 & x \in \Gamma \\ < 0 & x \in \Omega_2 \end{cases} \quad (28)$$

Here, the interface of interest is represented by the zero level-set of a function,  $\phi(x)$ . By using such a level set method, we can properly track the arbitrary fracture paths (both in the element and the boundary).

The stiffness of the standard element can be calculated with a Gaussian integral. The introduction of the discontinuity within

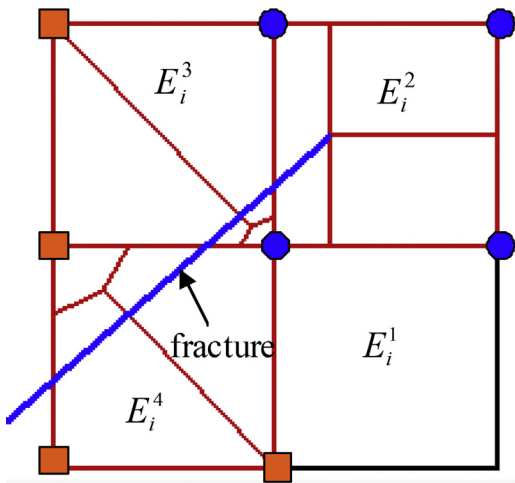


Fig. 4. The schematic of partition of unity in a cell with a fracture.

a cell element transforms the displacement and stress fields into highly nonlinear fields. In this case, the *partition of unity* (Dolbow, 1999) is used to obtain integral accuracy, and the cell element intersected by a crack or with a crack tip is divided by several quadrilateral subelements. Fig. 4 shows the typical partition of a cell, in which there is a cell element intersected by the crack ( $E_i^3$ ,  $E_i^4$ ), a cell element with the crack tip ( $E_i^2$ ), and a cell element near the crack surface, but without an intersecting crack ( $E_i^1$ ).

For mechanical processes, the local matrix can be deduced by using the principle of virtual work. The mechanical state is updated by using a local updating rule, which obviates the need to assemble and solve large-scale linear equations.

#### 4. Numerical tool—TOUGH-RDCA

Hydraulic fracturing in geological media is a coupled fluid flow and geomechanical problem. To solve such problems, researchers have employed both fully coupled and sequential implicit methods. In the former method, the flow and mechanics equations are solved simultaneously, providing unconditional and convergent numerical solutions. However, this method requires a unified flow-geomechanics simulator, which in turn requires a significant software development effort and could result in large computational costs. The sequential implicit method enables the use of existing

simulators for the solution of constituent subproblems. This is the approach taken in this study: we couple the two existing codes TOUGH2 and RDCA.

The sequential coupling scheme between TOUGH2 and RDCA can be found in the work by Pan et al. (2013), in which discontinuous behavior induced by multiphase flow is considered. This paper takes a further step by considering fracture propagation under a thermo-hydro-mechanical (THM) environment. Fig. 5 shows how fluid pressure is applied to the two opposite surfaces of a fracture, leading to stress concentration at the fracture tip. Once the stress at the fracture tip meets the failure envelope, propagation will occur. The effect of fluid flow on the fracture surfaces at different locations may be different (e.g., smaller pressure at the fluid front, as shown in Fig. 5b). The sequential coupling scheme of TOUGH-RDCA is an iterative two-way coupling that brings both modules to convergence.

In a coupled RDCA and TOUGH2 simulation, geometrically equivalent numerical grids are used. In RDCA, the numerical grid is independent of internal boundaries (Pan et al., 2012). Therefore, once an element is intersected by a propagating fracture, the element will be divided into several subelements based on the partition of unity, without the need to modify the original mesh. The mesh for the TOUGH2 model is equivalent to the original mesh of the RDCA model.

#### 5. Model verifications

To verify the ability of the TOUGH-RDCA code to model coupled fluid flow and geomechanics, including hydraulic fracturing, we present several test simulations here.

##### 5.1. Opening of static fracture induced by fluid pressure

We consider a plane-strain model domain 180 m × 180 m containing one fracture in the middle (Fig. 6). Different fracture lengths  $fl = 15, 17$ , and  $19$  m are considered. Fluid pressure within the fracture is uniform, and the magnitude is 10 MPa. The fracture opening along the fracture surface is monitored. Geomechanical properties, i.e., 6000 MPa for Young's modulus, and 0.3 for Poisson's ratio, are used. The simulation results (Figs. 7 and 8) show that, as expected, the fracture opening displacement (FOD) increases with increasing fracture length. The results are consistent with the analytical solution of the width of a static fracture in plane-strain geomechanics for a given net pressure, proposed by Sneddon and Elliot (1946).

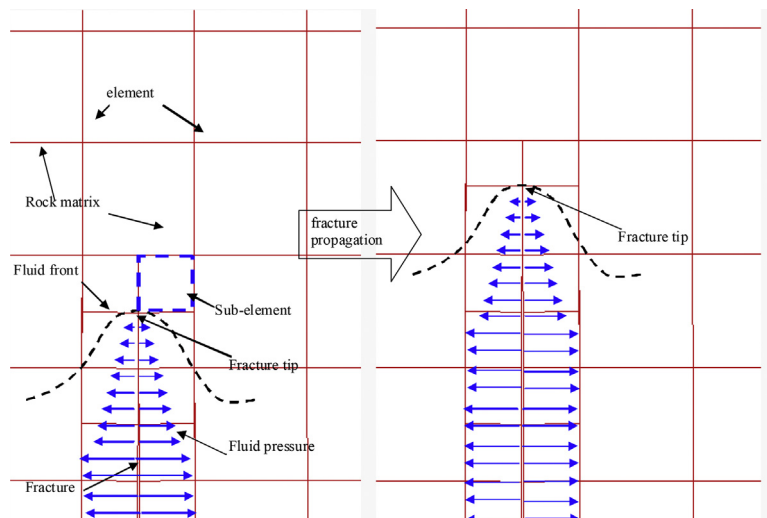


Fig. 5. The mechanical state of rock mass and fracture propagation induced by fluid flow.

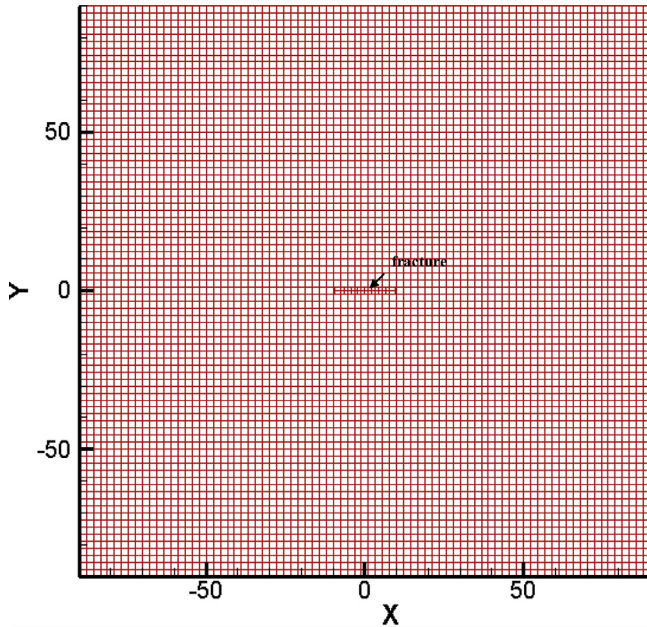


Fig. 6. Grid used in the modeling.

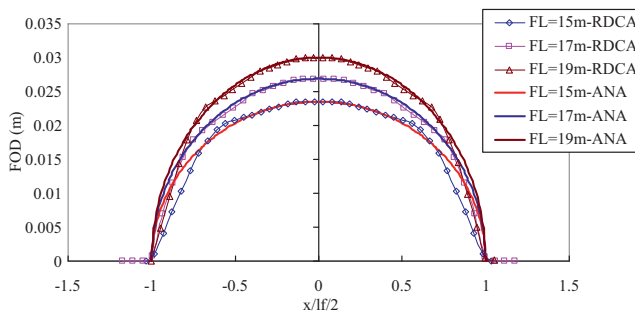


Fig. 7. Fracture opening Displacement (FOD) with different fracture lengths under fluid pressure.

### 5.2. Stress intensity factor

To verify the robustness of the RDCA for modeling fracture propagation under fluid injection, SIFs calculated by RDCA are compared with those from an analytical solution. The analytical solution of stress intensity factor  $K_I$  induced by the uniform internal pressure  $p$  within the crack surfaces can be found in a handbook of stress intensity factors (Sih et al., 1973). For an infinite plate with a crack,

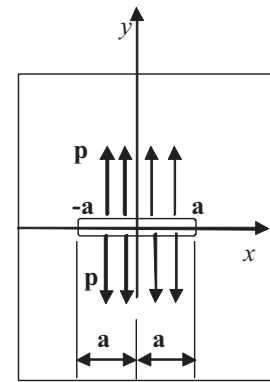


Fig. 9. An infinite plate with the effect of fluid pressure on crack surface.

as shown in Fig. 9, the stress intensity factor  $K_I$  with the effect of internal pressure can be expressed as

$$K_I = \frac{1}{\sqrt{\pi a}} \int_{-a}^a p \sqrt{\frac{a+x}{a-x}} dx \quad (29)$$

Let  $x = at$ , and we have

$$K_I = \frac{1}{\sqrt{\pi a}} \int_{-1}^1 p \sqrt{\frac{a+at}{a-at}} d(at) = p \sqrt{\frac{a}{\pi}} \int_{-1}^1 \sqrt{\frac{1+t}{1-t}} dt \quad (30)$$

Let  $t = \cos x$ , and we have

$$\begin{aligned} K_I &= p \sqrt{\frac{a}{\pi}} \int_{\pi}^0 \sqrt{\frac{1+\cos x}{1-\cos x}} d(\cos x) = -p \sqrt{\frac{a}{\pi}} \int_{\pi}^0 \sqrt{\frac{1+\cos x}{1-\cos x}} \sin x dx \\ &= -p \sqrt{\frac{a}{\pi}} \int_{\pi}^0 (1 + \cos x) dx = -p \sqrt{\frac{a}{\pi}} (x + \sin x) \Big|_{\pi}^0 = p \sqrt{\pi a} \end{aligned} \quad (31)$$

where  $a$  is half the length of the crack.

The model domain used in the RDCA simulation is 4 m × 4 m, with an initial vertical fracture in the rock mass (Fig. 10a). The bottom boundary is fixed for displacement normal to the boundary (roller). Mechanical and physical parameters are Young's modulus 20 GPa, Poisson ratio 0.2, thickness 1.0, and density 2263 g/m<sup>3</sup>. Fig. 10b shows the grid around the fracture where elements intersected by the fracture are discretized into subelements using partition of unity concept. Fluid pressure is applied at the crack surface at once, i.e., the fluid occupies the entire fracture space. Fig. 10c shows the SIF comparisons between the analytical solution and RDCA modeling. They are in close agreement, which verifies the RDCA code in the modeling of fracturing by fluid pressure.

### 5.3. Comparison of different fracturing criteria

Here, we conduct a comparison of the two criteria (i.e., a toughness-based criterion and a modified Mohr–Coulomb criterion

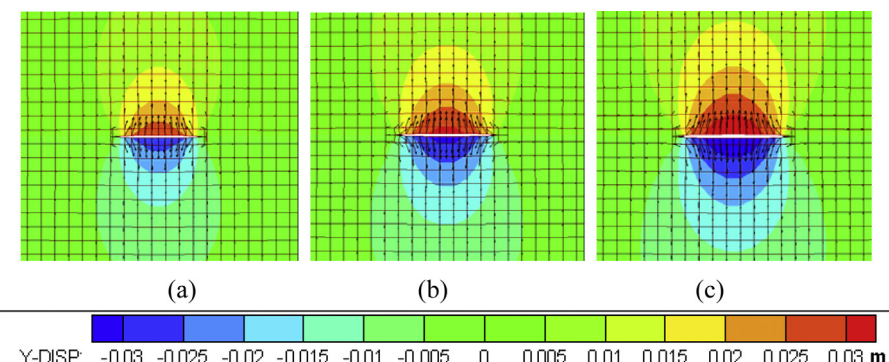
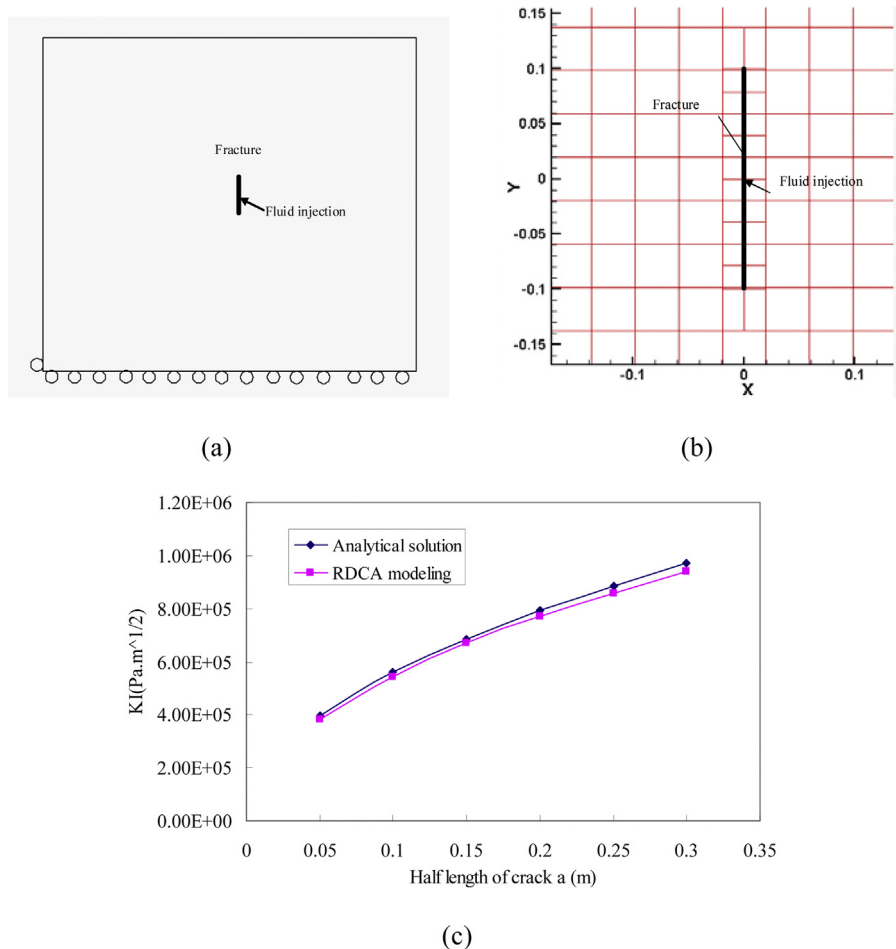


Fig. 8. Displacement in y direction and displacement vector of the fracture with different lengths. (a) 15 m; (b) 17 m and (c) 19 m.



**Fig. 10.** (a) Model used to calculate SIF by RDCA; (b) grid around fracture (with half length 0.1 m in this figure); (c) SIF KI comparisons between RDCA and an analytical solution.

with tension cut-off) when applied to the same problem of fracture propagation induced by fluid pressure. We use the numerical model shown in Fig. 6, which was previously used for comparison to analytical solutions of static fracture opening, but is used in this instance for modeling Mode I fracture propagation. We compare the results with the two fracture criteria in the case of  $E = 600$  MPa and  $\nu = 0.3$ . Our simulations show that for achieving fracture propagation at the same fluid pressure, the tensile strength applied in the modified Mohr–Coulomb model should be about twice the fracture toughness, i.e.,

$$\sigma_t = 2K_{IC} \quad (32)$$

Experimental studies (Zhang, 2002; Wang et al., 2007) have shown that the two parameters  $\sigma_t$  and  $K_{IC}$  of geomaterials including soils and rocks are linearly correlated by the equation  $\sigma_t = \alpha_p K_{IC}$ . However, the proportionality coefficient  $\alpha_p$  (unit:  $m^{-1/2}$ ) is different for different geomaterials and testing methods. In rock mechanics and rock engineering, the Mohr–Coulomb criterion with tension cut-off is widely used, because the parameters are more common and easy to determine experimentally. The Mohr–Coulomb criterion with tension cut-off is also the one used in the following simulation examples related to CO<sub>2</sub>-injection-induced caprock fracturing.

## 6. Applications to CO<sub>2</sub> injection into a brine formation

We demonstrated the capability of the RDCA-TOUGH simulator to model hydraulic fracturing through caprocks associated with

geologic CO<sub>2</sub> storage in deep sedimentary formations. Specifically, as shown in Fig. 11, we conducted modeling of CO<sub>2</sub> injection into a brine aquifer overlain by multiple caprocks and aquifers. In these hypothetical modeling examples, we intentionally raised the injection pressure sufficiently to induce fracture propagation through the caprock. This was done to test the applicability of the modeling approach and (at the same time) to study potential monitoring options that could be used to detect such fracturing at a real site. We conducted simulation cases considering caprock that may contain a few fractures that could be propagated upon pressurization (see fractures F1, F2, and F3 in Fig. 11), and in some cases we

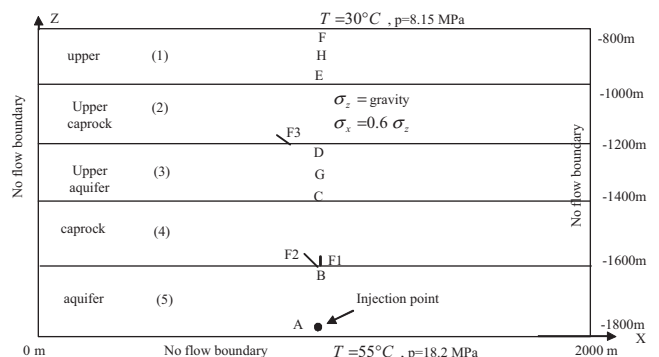


**Fig. 11.** Model description.

**Table 1**  
Rock matrix material properties.

Property	Upper	Upper caprock	Upper aquifer	Caprock	Aquifer
Young's modulus, $E$ (GPa)	5	5	5	5	5
Poisson's ratio, $\nu$ (-)	0.25	0.25	0.25	0.25	0.25
Biot's parameter, $\xi$ (-)	1	1	1	1	1
Saturated rock density, $\rho_s$ (kg/m <sup>3</sup> )	2260	2260	2260	2260	2260
Zero stress porosity, $\phi_0$ (-)	0.1	0.01	0.1	0.01	0.1
Residual porosity, $\phi_r$ (-)	0.09	0.009	0.09	0.009	0.09
Zero stress permeability, $k_0$ (m <sup>2</sup> )	1e-15	1e-17	1e-13	1e-17	1e-13
Corey's irreducible gas saturation, $S_{rg}$ (-)	0.05	0.05	0.05	0.05	0.05
Corey's irreducible liquid saturation, $S_{rl}$ (-)	0.3	0.3	0.3	0.3	0.3
van Genuchten's air-entry pressure, $P_0$ (kPa) (at zero stress)	196	3100	19.6	3100	19.6
van Genuchten's exponent, $m$	0.457	0.457	0.457	0.457	0.457
Cohesion (MPa)	2	2	2	2	2
Friction angle (degree)	28	28	28	28	28
Tensile strength (MPa)	0.1	0.1	0.1	0.1	0.1

compared the results to a case of a homogeneous competent caprock in which no fracturing takes place.

### 6.1. Model setup, input parameters, and simulation cases

We conducted these simulations using a 2-dimensional plane-strain model domain that extended vertically from 800 m to 1800 m in depth and 2 km horizontally (Fig. 11). The model geometry was designed for focusing our analysis on upward fracturing at the central part of the model. We simulated injecting CO<sub>2</sub> into the lower aquifer at a constant rate of 0.05 kg/s per meter per meter normal to the model plane. This flow rate is equivalent to 1.6 Mt/year if the injection were conducted along a 1000 m thick section of the reservoir normal to the model plane (for example, representing the injection rate for a 1 km long horizontal well). We considered this a realistic injection rate. For example, at the In Salah CO<sub>2</sub> storage project, injection rates have been 0.5–1.0 Mt/year distributed over three horizontal injection wells, each 1–1.5 km long (Rutqvist et al., 2010). Using such an injection rate, the pressure in the injection aquifer increases at such a rate that fracturing occurs within 1 year.

No flow is assumed at the left, right, and bottom boundaries (Fig. 11). Initially, with the domain subject to a gravity field in the vertical direction, we apply a vertical stress on top of the model corresponding to the weight of the overburden. The sediments above 800 m could be excluded from the model, assuming that they are much softer, e.g., having much smaller shear modulus. The horizontal stress is assumed to be a factor 0.6 of vertical stress, i.e.,  $\sigma_x = 0.6\sigma_z$ . Gradients of pore pressure and temperature are assigned to the entire model. The temperature is assumed to be 10 °C on the ground surface with a gradient of 25 °C/km, whereas a hydrostatic pressure gradient is assumed with the groundwater table coinciding with the ground surface.

These gradients result in temperature and pressure values at the top and bottom boundaries as shown in Fig. 11. Moreover, at a depth of 1600 m, the pore pressure and temperature are about 16.1 MPa and 40 °C, and the stresses are  $\sigma_x = -21.3$  MPa, and  $\sigma_z = -35.4$  MPa. Thus, the horizontal stress is the minimum compressive stress, and we could therefore expect that the injection fluid pressure should increase above 21.3 MPa for vertical fracturing to be initiated. We note that the selected stress field ( $\sigma_x = 0.6\sigma_z$ ), corresponds to a lower-bound least-principal compressive stress for a crust critically stressed for shear in favorably oriented faults (Zoback, 2007), although even smaller values are possible (Zang and Stephansson, 2008). We select this normal-faulting stress regime as an unfavorable case in terms of the potential for inducing vertical fracture propagation through caprock. As an example of a horizontal stress

approximately 0.6 of the vertical, we refer to the In Salah CO<sub>2</sub> injection site in Algeria (Rutqvist, 2012).

The model domain is discretized into a two-dimensional plane-strain model (2 km × 1 km) with 20,000 uniform elements (size 10 m × 10 m). Table 1 lists the material parameters of rock matrix. The rock properties listed in Table 1, e.g., permeability for the different rock units, are taken from Rutqvist and Tsang (2002) and correspond to sandstone aquifers and caprocks of shale. The parameters for the porosity-mean stress and permeability-porosity relationship— $\phi_0$ ,  $\phi_r$ ,  $\alpha$ ,  $c$  in Eqs. (11) and (13)—were determined in Rutqvist and Tsang (2002) by fitting to experimental laboratory data on sandstone samples, and then adjusting for the shale layers to match experimental stress-versus-permeability relations for shale shown in Rutqvist and Stephansson (2003). Elastic properties are (for simplicity) taken to be the same for all layers, from the ground surface to the bottom of the model. In reality, the Young's modulus is generally expected to increase with depth, and the selected values of the Young's modulus could be considered a lower range value at the depth of injection. The main differences between the aquifer and shale layers were the hydraulic properties, i.e., porosity, permeability, capillary pressure, and relative permeability. Caprock permeability was 4 orders of magnitude less than aquifer permeability, even though the caprock permeability value used in this study is in the upper range. For fractures, the normal stiffness was  $K_n = 500$  GPa/m, the shear stiffness  $K_s = 10$  GPa/m, and the friction coefficient 0.3.

The ECO2N fluid property module (Pruess and Spycher, 2007) is employed for modeling the thermodynamic and thermophysical properties of water–NaCl–CO<sub>2</sub> mixtures. The relative permeability of gas and liquid phases is calculated from Corey's function (Corey, 1954), while capillary pressure was governed by van Genuchten's function (van Genuchten, 1980). Detailed model description and parameters can be found in the work by Rutqvist and Tsang (2002). The fracture properties given in this section are related to two rough fracture surfaces in contact. As long as there is a fracture surface-to-surface contact, the elastic shear and normal displacement depends on the fracture normal stiffness and shear stiffness, whereas the potential for shear slip depends on the internal friction angle. If the fracture opens to such a degree that there is a complete loss of fracture surface-to-surface contact, the mechanical response of the fracture depends on the elastic properties of the surrounding rock, as well as on the properties related to fracture propagation.

In model simulations, we considered four different cases: Case 0: No initial fracture; Case 1: with initial fracture F1; Case 2: with initial fracture F2; Case 3: with initial fractures F2 and F3. First, we studied Case 1, involving the vertical fracture F1 at the bottom of the lower caprock. Thereafter, we considered Cases 2 and

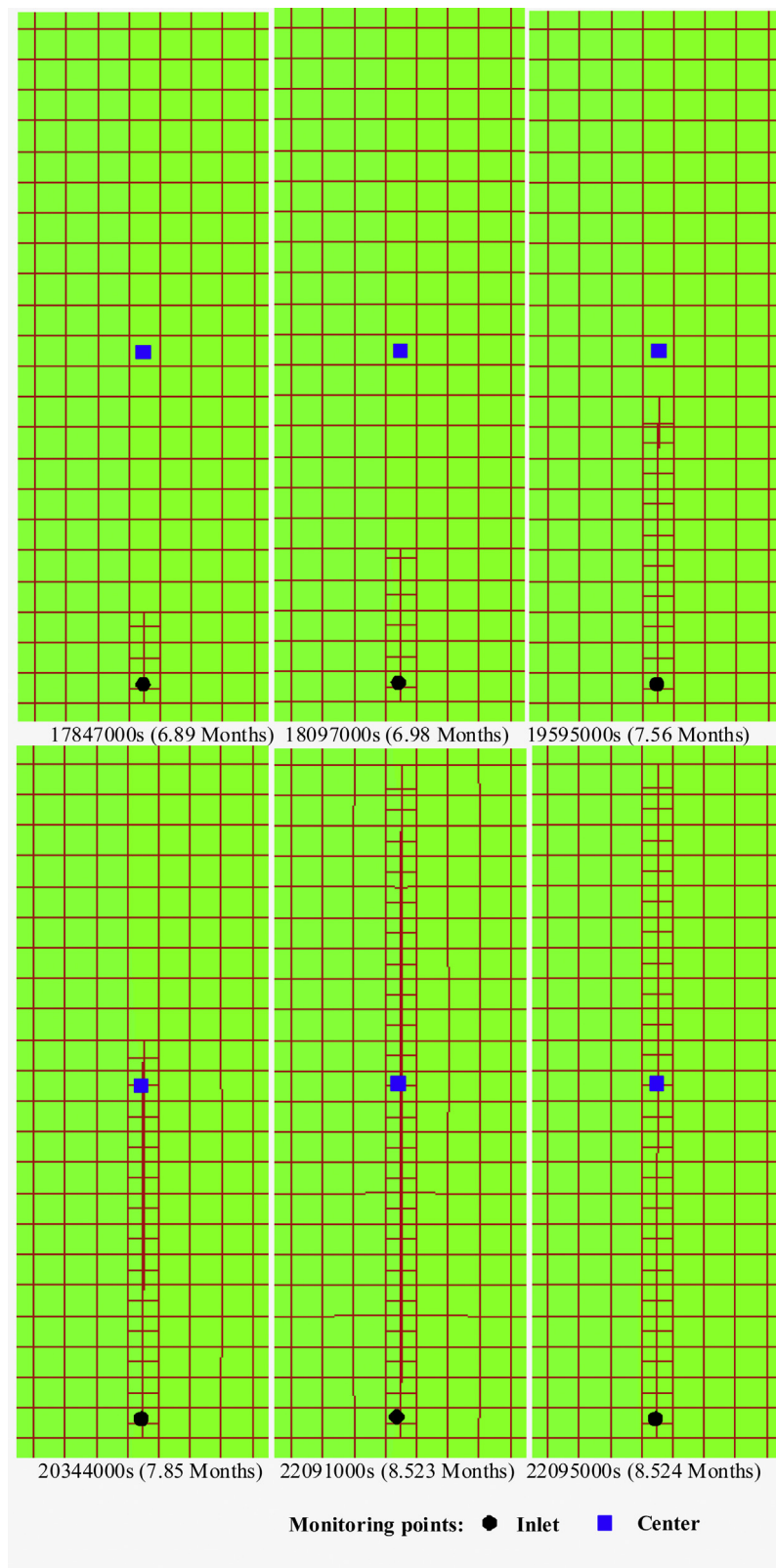


**Fig. 12.** Fracture propagation in caprock with initial vertical fracture during the injection of CO<sub>2</sub>.

Case 3, which involved inclined fractures F2 and F3, and we compared the simulation results for the different cases. In the modeling, the pore pressure, saturation, and displacement at different points were monitored (see A, B, C, and D in Fig. 11), as were the fracture opening and shear displacement.

#### 6.2. Results for a single vertical fracture F1 (Case 1)

For Case 1, we consider an initial fracture F1 in the lowermost part of the lower caprock, whereas the upper caprock is assumed homogenous and unfractured. Fracture F1 is 20 m long

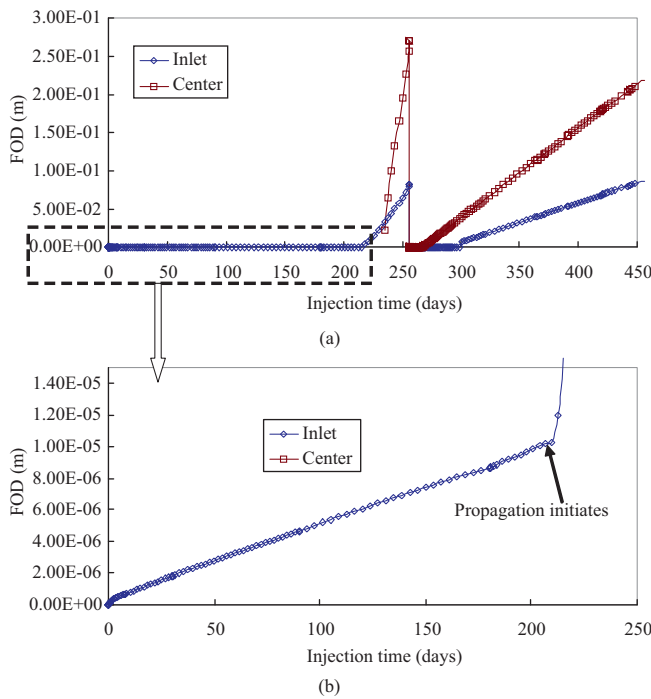


**Fig. 13.** Fracture opening displacement evolution at inlet and the penetrated fracture center position during  $\text{CO}_2$  injection (Inlet and Center mean the monitoring points shown in Fig. 12).

and assumed to be closed initially, i.e., the permeability of the fracture is the same as the ambient rock mass. During injection of  $\text{CO}_2$ , the aquifer fluid pressure increases, and as a result, the effective stress decreases. At the same time, the fracture in the lower part of the caprock opens, because of the increase in aquifer fluid pressure, and fluid can diffuse into the fracture, which will then undergo a pressure increase. The stress concentration at the fracture tip will increase in response to the increasing internal fluid pressure. Once the stress at the tip exceeds the strength defined by the failure criterion, the fracture will propagate.

Fig. 12 through Fig. 17 show the simulation results for Case 1. Fig. 12 shows the discontinuous fracturing process of the fracture in the caprock during the injection of  $\text{CO}_2$ . When the fracture breaks through the caprock at 255.68 days, the fracture closes for a short time. As shown in Figs. 13 and 14, the aquifer pressure (points A and B) gradually increases until fracture propagation initiates after about 207 days of  $\text{CO}_2$  injection. During this initial phase of pressure increase without fracture propagation, the fracture opens as a result of decreasing effective stress within the existing fracture. For example, at point B, located at the inlet of fracture F1, the fracture opens about 10  $\mu\text{m}$  while the pressure increases about 7.5 MPa

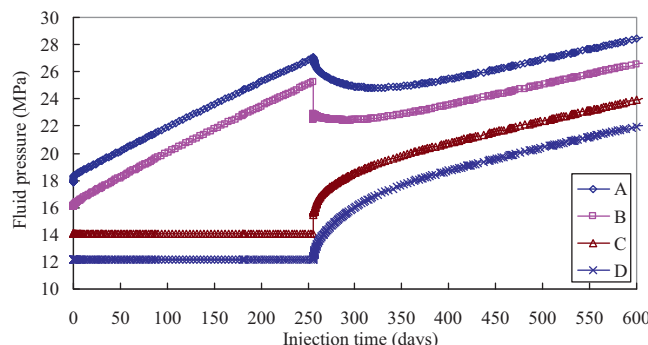


**Fig. 14.** Fluid pressure evolution at different points during  $\text{CO}_2$  injection.

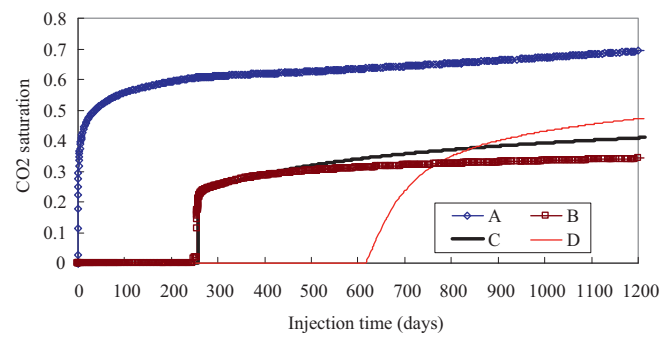


**Fig. 15.**  $\text{CO}_2$  saturation evolution at different points during injection.

(from 16 to 23.5 MPa). At 207 days, at the instant when the fracture starts to propagate, the fluid pressure in point B has reached about 23.5 MPa, which is a few MPa higher than the minimum compressive stress at that point. Because the initial fracture is vertical and the minimum compressive stress is horizontal, Mode I fracture propagation occurs. The fracture propagation takes place in a stable manner until 255.68 days, when the fluid pressure at the inlet of the fracture is about 25 MPa. At Point A, the (injection) pressure is about 25.2 MPa at fracture initiation and 27 MPa at caprock breakthrough.

At the instant when the fracture starts to propagate, i.e., about 207 days, there is a sharp increase in the rate of fracture opening (Fig. 13). This sharp increase in displacement occurs despite the fact that the fluid pressure still increases gradually and continues to increase gradually until 256 days, when the fracture breaks through the entire caprock into the overlying aquifer (Point B in Fig. 14). The sharp increase in opening is caused by a loss of fracture surface-to-surface contact, when the fluid pressure within the fracture exceeds the compressive stress normal to the fracture. The loss of fracture surface-to-surface contact translates into a loss of mechanical stiffness that results in a higher rate of fracture opening. Interestingly, during this fracture-propagation phase, the fracture opening at the center point of the fracture becomes much larger than the inlet point (see Fig. 13a). This shows that once there is a complete loss of fracture surface-to-surface contact, the fracture opening occurs and is similar to that shown in Fig. 7, i.e., with the largest opening taking place at the center of the crack.

Once the caprock is fully penetrated by the propagating fracture (at 256 days), a sudden decrease of the fluid pressure is observed in the lower aquifer (see the pressure evolution at points A and B in Fig. 14). The most abrupt pressure decrease occurs at the inlet of the fracture, where the fluid pressure decreases from about 25 MPa to about 22 MPa. This abrupt pressure decrease is caused by the release of fluid into the overlying aquifer, which is then gradually pressurized (see the pressure evolution at points C and D in Fig. 14). As a result of the sudden pressure decrease at the fracture inlet, the fracture closes suddenly, and fracture surface-to-surface contact is again achieved (Fig. 13). Moreover, as fluid is released into the upper aquifer,  $\text{CO}_2$  moves quickly up from the injection, by buoyancy through the fracture, and reaches the upper aquifer (see the evolution of  $\text{CO}_2$  saturation at point C in Fig. 15). In fact, the sharp pressure decrease at the inlet of the fracture might be strongly impacted by the increased fluid mobility inside the fracture once the native brine is replaced with a lower viscosity  $\text{CO}_2$ —an effect that was also observed in simulations of fault leakage by Rutqvist and Tsang (2002).

With continuous  $\text{CO}_2$  injection, the pore pressure gradually recovers because of continuous, significant fluid release into the overlying aquifer (Fig. 14), and after some time the fracture once again starts to open. Then, after a short time, the fracture opens continuously with increasing fluid pressure and, as a result, the fracture

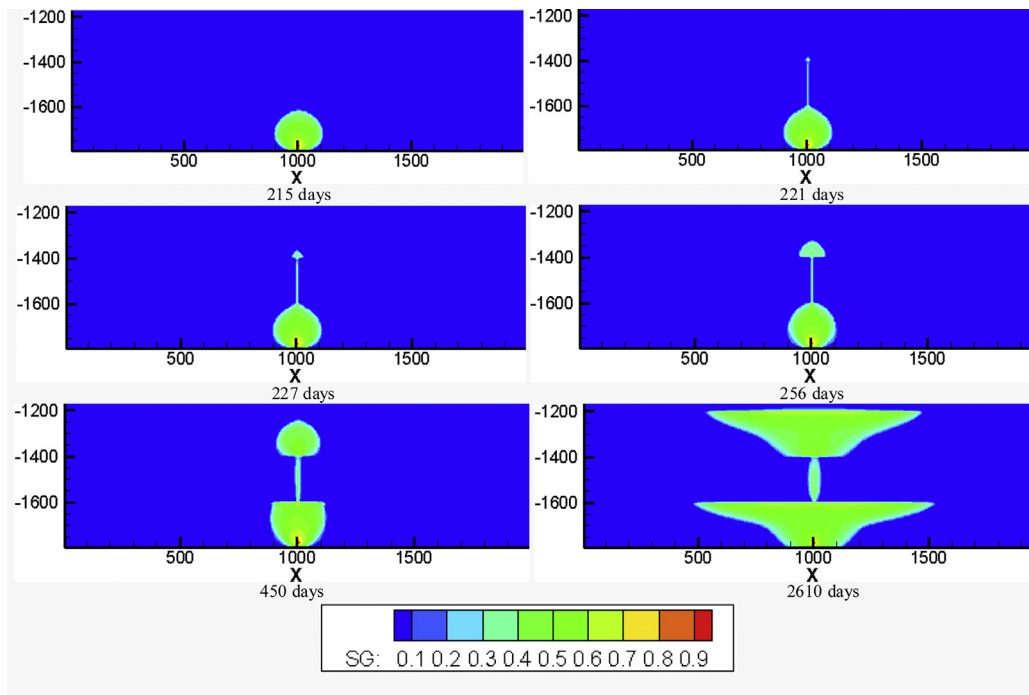


**Fig. 16.** CO<sub>2</sub> saturation evolution.

permeability increases, leading to an ever increasing release rate of CO<sub>2</sub> into the overlying aquifer. For example, Fig. 15 shows how CO<sub>2</sub> reaches Point D at the top of the overlying aquifer after 617 days.

Fig. 16 shows the spread of the CO<sub>2</sub> plume up to 2610 days. As seen from the contour, the CO<sub>2</sub> plume migrates along the created fracture through the caprock at about 221 days. Although the permeability of the caprock is much lower than that of the aquifer, a small amount of CO<sub>2</sub> seeps into the caprock around the fracture. The displacement at points B and C drops suddenly after the penetration of the fracture (see displacement evolution at points B and C in Fig. 17). Thereafter, the displacements at these two points increase gradually, because of the recovery of fluid pressure in the lower aquifer. The vertical displacement in the upper caprock increases suddenly after CO<sub>2</sub> migrates into the upper aquifer through the penetrated fracture (see displacement evolution at points D and E in Fig. 17).

### 6.3. Results for inclined fractures F2 and F3 (Case 2 and Case 3)

For Case 2, we replace vertical fracture F1 with fracture F2, which is 83 m long and dips 75 degrees. For Case 3, we keep F2, but add fracture F3 (with the same dimensions and dip) at the

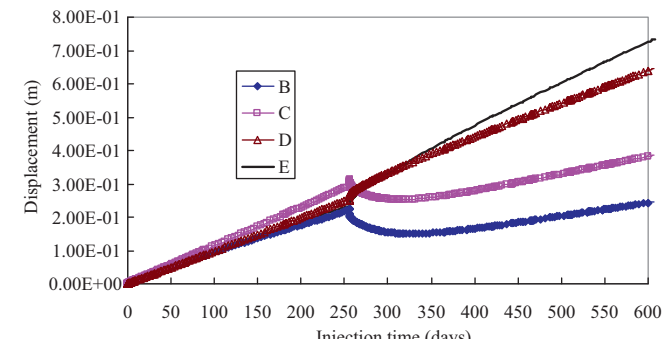


**Fig. 17.** Vertical displacement evolution at different points.

upper caprock. In both Case 2 and Case 3, fracture F2 would first start to propagate, but as long as F2 did not propagate all the way through the lower caprock, the coupled fluid flow and geomechanical behavior for Case 3 were identical to that of Case 2.

Fig. 18a shows the propagation of the initial fracture in the lower caprock for Case 2. With the injection of CO<sub>2</sub>, the initial fracture is activated (i.e., stick, open, and slide). The slide (or shear activation) of the initial fracture leads to a stress concentration at the fracture tip, with propagation starting after 134 days of injection. As can be observed from the fracturing process, the fracture turns and propagates along the direction parallel to the direction of the maximum compressive stress, i.e., in this case, the vertical direction. At 190 days, the fracture propagates across the lower caprock. Similar to Case 1, before breakthrough, the fracture opens gradually because of the fluid-pressure increase induced by CO<sub>2</sub> injection. After that, the fracture closes temporarily due to the decrease in fluid pressure at the lower aquifer and then opens again, continuously, because of the continuous injection of CO<sub>2</sub> and fluid-pressure recovery.

For Case 3, before 190 days (time of breakthrough within the lower caprock), the fracturing behavior is similar to Case 2. When the CO<sub>2</sub> migrates to the upper aquifer, the initial fracture in the upper caprock undergoes a stick, open, slide (shear activation), and propagation process, owing to the increase in fluid pressure (Fig. 18b). Finally, the fracture propagates across the upper caprock, and the CO<sub>2</sub> plume could eventually migrate upwards through the fracture, towards shallower aquifers and the ground surface.

Figs. 19 and 20 show comparisons between the displacement and fluid pressure evolutions for different simulation cases. In all cases, the displacement evolution is strongly related to the evolution of fluid pressure. For the homogeneous caprock case (Case 0), because there is no fluid leakage across the caprock, and consequently the aquifer pressure increases linearly with time, the aquifer, pressurized by the injection, expands vertically and lifts up the overburden rock continuously, although not exactly linearly. For caprocks with pre-existing fractures, the breakthrough of the caprock by fracturing greatly affects the evolution of displacement and fluid pressure. Right after the breakthrough, the fluid pressure drops quickly and results in some subsidence. Numerical results

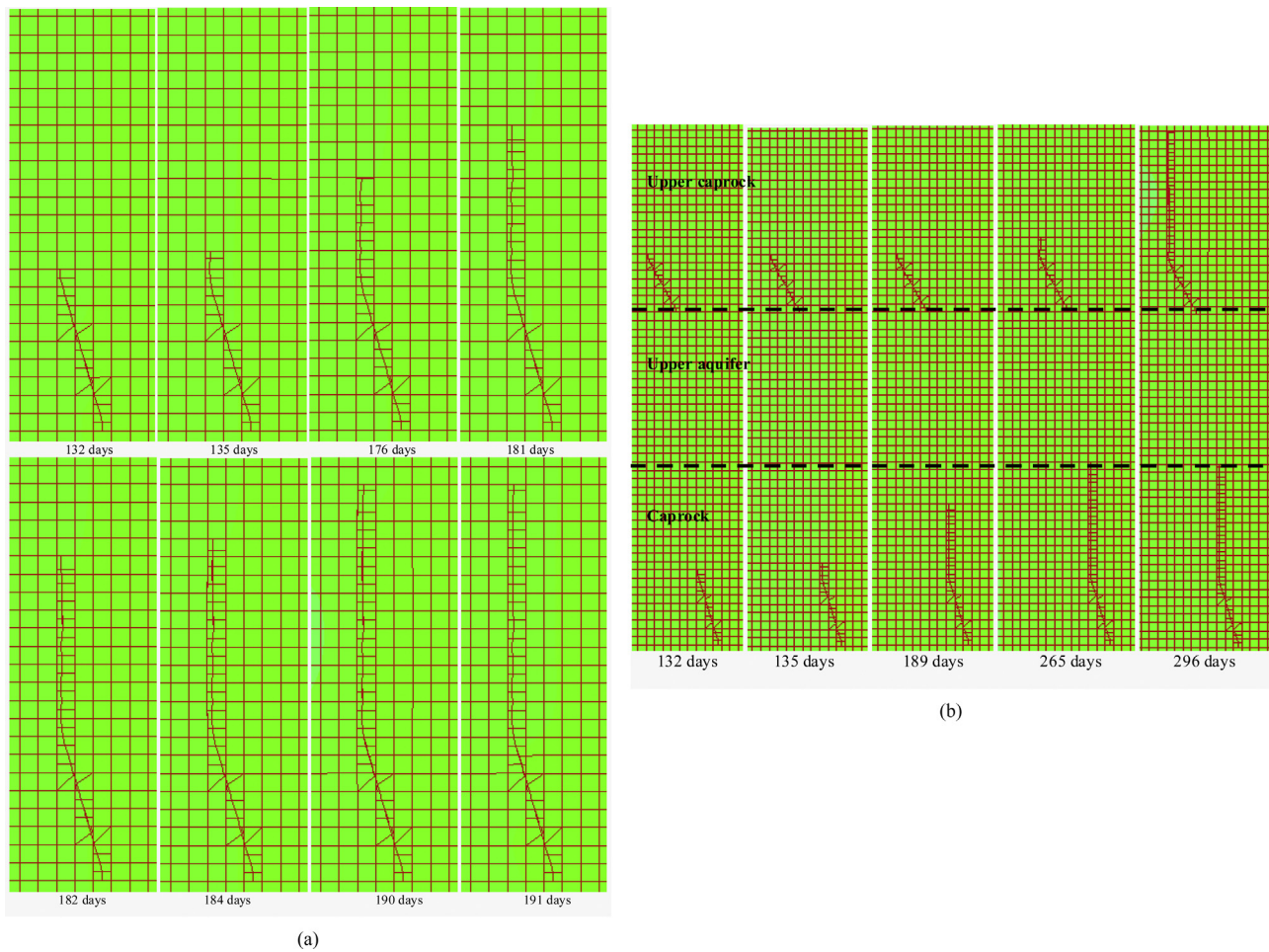


**Fig. 18.** Fracture propagation in caprock with initial slant fracture during the injection of CO<sub>2</sub>. (a) Case 2 and (b) Case 3.

show that the initiation and propagation of fractures for Case 2 and Case 3 occurs earlier and at a few megapascals lower aquifer pressure than for Case 1.

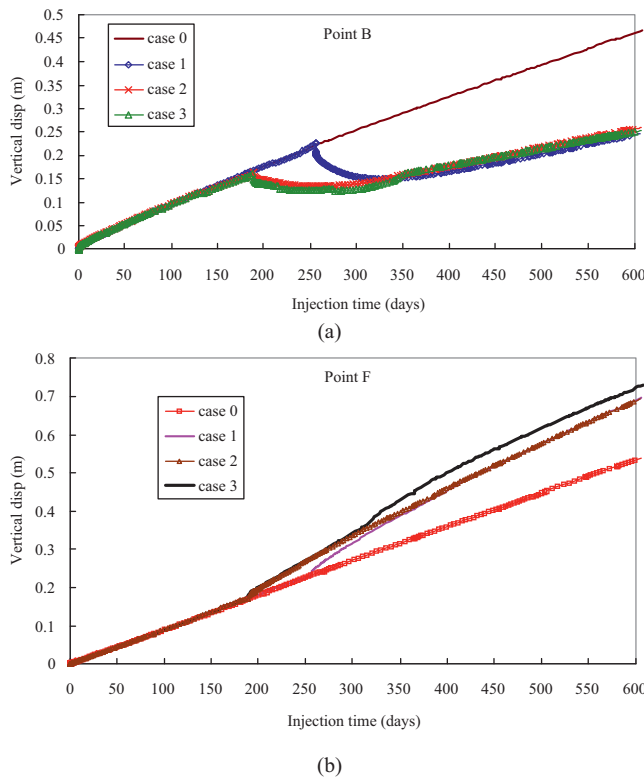
In all cases with pre-existing fractures, the injection of CO<sub>2</sub> leads to an increase in fluid pressure and decrease in effective normal stress within the fracture. In the cases involving a slanted fracture (Case 2 and Case 3), the reduction in effective stress within the fracture surfaces leads to a loss of frictional shear strength. Eventually, when the frictional shear strength becomes less than the applied (tectonic) shear stress, the fracture will slide. Actually, the initial fractures slide at the beginning of the injection (Fig. 21). The sliding and opening of the initial fracture induces a severe stress concentration at the fracture tip. For the vertical fracture in Case 1, the stress concentration at the fracture tip is caused solely by fracture opening.

Fig. 22 presents comparisons of CO<sub>2</sub> saturation for different cases at different injection times, showing how the initial fracture and its propagation affect CO<sub>2</sub> plume migration. We found that, for the homogeneous case (Case 0), the CO<sub>2</sub> plume extends about 400 m away from the injection point in the lower aquifer after 270 days. For the heterogeneous cases (Case 1, Case 2, and Case 3), the CO<sub>2</sub> plume extends 350 m away from the injection point in the lower aquifer after 1186 days, because of the leakage of CO<sub>2</sub> through the fractures. For Case 3, the CO<sub>2</sub> plume reaches the upper rock mass through the fracture in the upper caprock, and could potentially migrate up to shallower aquifers and the ground surface. Thus, from these simulation cases, we observe the important impact that material heterogeneities, such as damage and pre-existing fractures, can have on caprock sealing performance.

## 7. Discussion on safe injection pressure and potential monitoring

Future regulations related to underground CO<sub>2</sub> injection might limit the admissible injection pressure to the fracturing gradient just above the intended storage zone, as evaluated by leak-off or mini-frac tests in the caprock. For example, with respect to U.S. regulatory standards regarding the deep injection of liquid waste, it is the current practice to keep the maximum injection pressure less than the measured fracture-closure pressure of the caprock. Below that fracture-closure pressure, no existing fractures can open, and no new fractures can form, implying no enhanced migration of waste fluids out of the injection intervals (USEPA, 1994). However, in the case of potential future commercial CO<sub>2</sub> injections from an emitting power plant, injection would take place at a much larger scale, and therefore other issues, such as the potential for fault reactivation, or long-term sealing performance, may be limiting factors on the admissible overpressure (Rutqvist, 2012).

In our study, we did not consider the potential for reactivation of larger faults. Nevertheless, we found that shear reactivation of pre-existing fractures that might exist in an otherwise competent caprock might well be an important issue for caprock seal integrity, as well as for estimating the maximum sustainable injection pressure. The importance of shear reactivation of existing fractures, as a lower limit for a sustainable injection pressure, was highlighted already by Rutqvist and Tsang (2002), and applied by Lucier et al. (2006). Here, we have performed simulation studies that show how such shear reactivation could occur at a relatively



**Fig. 19.** Displacement evolution comparisons between different cases at different points. (a) Point B (below lower caprock) and (b) Point F (top of upper rock).

low injection pressure—and how shear slip could also promote fracturing to create a new flow path up through a caprock unit.

Given this consideration, we may also consider some different criteria for estimating a maximum sustainable injection pressure. The lithostatic stress is a parameter that can be easily estimated quite accurately from the weight of the overburden rock, whereas the most relevant stress parameter, the least principal stress, requires *in situ* measurements using specialized equipment or other means of bounding estimates (Zoback, 2007; Zang and Stephansson, 2008). From our simulation results, we can conclude that the fracturing of the caprock was initiated at an injection pressure far less than the lithostatic stress. Indeed, in this case, the lithostatic stress at 1600 m depth would be estimated from the weight of the overburden to be about 35.5 MPa, whereas fracturing was initiated at an injection pressure of about 25 MPa for Case 1 and 23 MPa for Case 2 and Case 3. The minimum compressive stress, i.e., the horizontal stress at 1600 m, was  $-35.5 \times 0.6 = -21.3$  MPa. Thus, in both cases, the injection pressure exceeded the minimum principal stress.

Another criterion for maximum sustainable injection pressure might be to consider shear reactivation that conservatively could take place in an unknown fracture having an arbitrary orientation. Note that fractures of these dimensions, i.e., single plane fractures of an initial aperture less than a millimeter and extending tens of meters, would not be detectable by site characterization, unless they happen to be intersected by an exploratory well. With this in mind, one conservative approach might be to assume that such undetected fractures of any orientation could exist. Using a Coulomb friction criterion, and assuming cohesionless fractures having a friction coefficient of 0.3, the critical pressure could be stated as follows (Rutqvist et al., 2007):

$$P_c = \frac{1.81\sigma_3 - \sigma_1}{0.81} \quad (37)$$

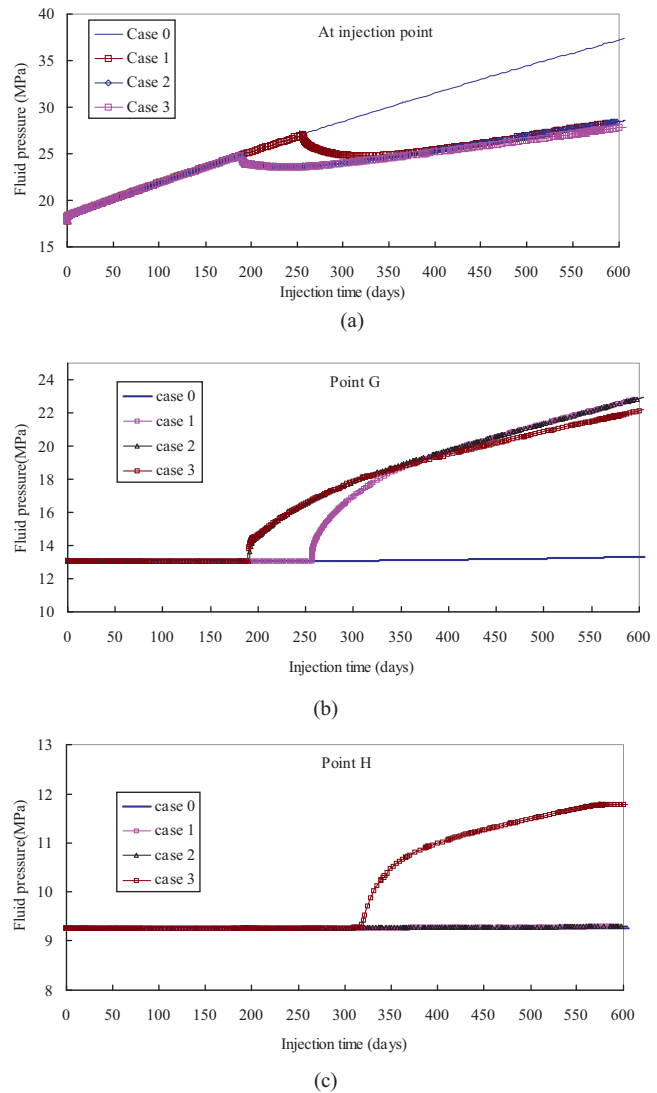


**Fig. 20.** comparison of pore pressure evolution between different cases at different places. (a) Injection point; (b) Point G (1000 m, -1295 m) at upper aquifer and (c) Point H (1000 m, -915 m) at upper rock.

In the current case, a critical injection pressure is 4.4 MPa, which is much lower than the initial fluid pressure in the lower aquifer. This means that fractures optimally oriented for shear slip would be in a state of shear slip already at initial stress. However, as long as the fracture does not propagate, this shear slip is local and cannot by itself provide a new flow path through the caprock. Thus, in this case, maximum sustainable injection pressure based on the shear

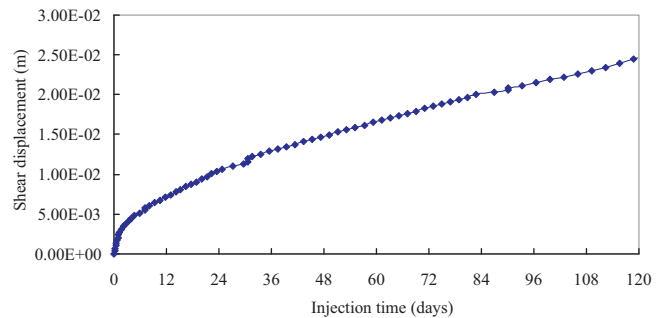


**Fig. 21.** shear displacement evolution of slant fault during injection.

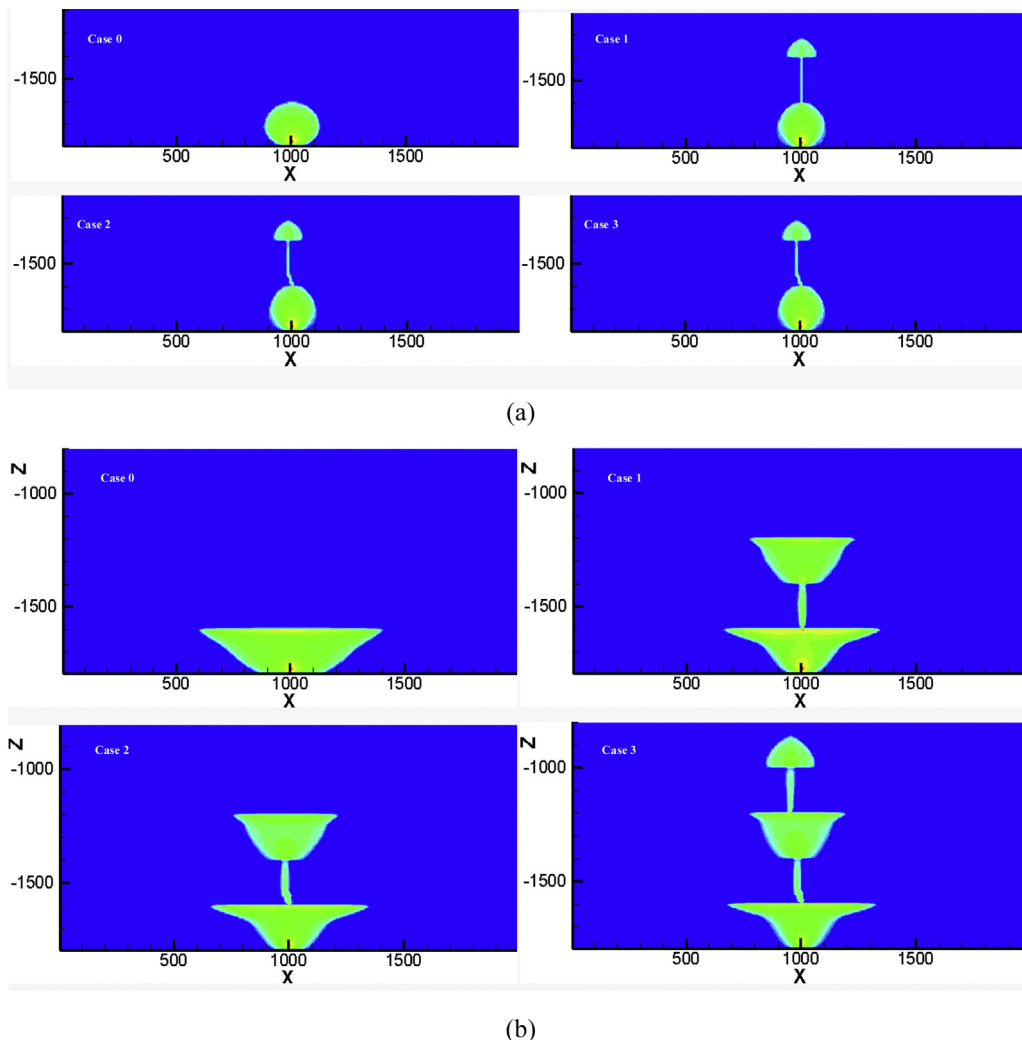


**Fig. 22.** CO<sub>2</sub> Saturation contours of different cases at different injection time. (a) 270 days and (b) 1186 days.

slip criterion in Eq. (37) would be too conservative; a criterion based on the minimum principal stress would be more appropriate.

Moreover, in this case we considered a normal faulting stress regime unfavorable for inducing vertical fractures and shear activation on steeply dipping fractures. A reverse faulting stress regime (with the horizontal stress being higher than the vertical) could effectively prevent vertical fracturing and shear reactivation on steeply dipping fractures. However, such a regime could possibly result in horizontal fractures and reactivation along shallowly dipping faults that would be much less likely to propagate vertically across the caprock (Rutqvist et al., 2008). However, the stress regime selected in this study is not unrealistic, and is in fact close to that of the In Salah CO<sub>2</sub> storage project, at which fracturing or opening of a vertical fracture zone seems to have occurred in the caprock at a depth of about 1800 m (Rutqvist, 2012; Rinaldi and Rutqvist, 2013).

Finally, our simulations were conducted using the isotropic and homogeneous mechanical properties of each layer, whereas in the field, different stiffness and strength properties for each layer can provide strength or stress barriers for fracture propagation. At a real site, it will be important to consider such contrasting properties in the different layers, because they can significantly impact the overpressure required to induce fracturing.

Our simulation results are also relevant for investigating potential monitoring methods for detecting caprock leakage through

hydraulic fracturing. In our simulations, we observed distinct responses in fluid pressure and vertical displacements as soon as fractures broke through the lower caprock. However, there was no obvious indication in injection pressure or displacement before such a breakthrough. That is, the fracturing of the lower caprock can proceed unnoticed for several months of injection. The distinct responses in pressure and vertical displacement upon caprock breakthrough would be a good indicator, one that could be used at a real site for taking preventative action (such as shutting down the injection). In such a case, shallow aquifers would still be protected by the additional caprock layers.

## 8. Concluding remarks

In this paper, we present and demonstrate a coupling of two numerical codes—a rock discontinuous cellular automaton (RDCA) for geomechanics, and TOUGH2, a numerical simulator for modeling nonisothermal and multiphase fluid flow—to simulate caprock fracturing during high-pressure CO<sub>2</sub> injection into a brine aquifer. The RDCA code uses an integration of several techniques (e.g., fracture mechanics, partition of unity, and level set method) to simulate and capture the fracturing behavior of a rock mass. The most important feature of this code is that the numerical grid and internal boundaries (e.g., fractures) are independent of each

other. Therefore, the code is suitable and convenient for simulating fracture propagation and for use in coupled analysis with TOUGH2.

We demonstrate the ability of this coupled method to simulate fracturing processes, including hydraulic fracture propagation under the multiphase fluid-flow conditions. With respect to geologic CO<sub>2</sub> storage, our study highlights the role of initial caprock damage, such as natural fractures, and how such damage could impact caprock sealing integrity. With initial damage or fractures in the lower part of the caprock, injection-induced pressure can diffuse into the fracture and potentially propagate upwards across the caprock, creating a new flow path for CO<sub>2</sub> to migrate out of the intended storage aquifer. Moreover, our modeling results also show how an inclined fracture could reactivate in shear, which thereby could promote fracture propagation at a slightly lower pressure.

However, our modeling also showed that, in order to maintain caprock sealing integrity, an injection pressure limited by minimum principal stress is required. Finally, the importance and usefulness of pressure and deformation monitoring, which could potentially be effective techniques for early detection of fracture propagation breaking through a caprock layer are highlighted.

## Acknowledgments

This work was financially supported by the National Natural Science Foundation of China under Grant Nos. 51322906 and 41272349, and the National Basic Research Program of China under Grant No. 2010CB732006, and in part, supported by the U.S. Dept. of Energy under contract No. DE-AC02-05CH11231.

## References

- Adachi, J., Siebrits, E., et al., 2007. Computer simulation of hydraulic fractures. *International Journal of Rock Mechanics and Mining Sciences* 44 (5), 739–757.
- Atkinson, B.K., 1987. *Fracture Mechanics of Rocks*. Academic Press Inc, Orlando, FL.
- Belytschko, T., Black, T., 1999. Elastic crack growth in finite elements with minimal remeshing. *International Journal for Numerical Methods in Engineering* 45 (5), 601–620.
- Bissell, R., Vasco, D., et al., 2011. A full field simulation of the In Salah gas production and CO<sub>2</sub> storage project using a coupled geo-mechanical and thermal fluid flow simulator. *Energy Procedia* 4, 3290–3297.
- Boone, T.J., Ingraffea, A.R., 1990. A numerical procedure for simulation of hydraulically-driven fracture propagation in poroelastic media. *International Journal for Numerical and Analytical Methods in Geomechanics* 14 (1), 27–47.
- Bower, K.M., Zywoloski, G., 1997. A numerical model for thermo-hydro-mechanical coupling in fractured rock. *International Journal of Rock Mechanics and Mining Sciences* 34 (8), 1201–1211.
- Bredehoeft, J., Wolff, R., et al., 1976. Hydraulic fracturing to determine the regional in situ stress field, Piceance Basin, Colorado. *Geological Society of America Bulletin* 87 (2), 250–258.
- Broek, D., 1982. *Elementary Engineering Fracture Mechanics*. Springer, The Hague, The Netherlands.
- Carrier, B., Granet, S., 2012. Numerical modeling of hydraulic fracture problem in permeable medium using cohesive zone model. *Engineering Fracture Mechanics* 79 (0), 312–328.
- Carter, B., Desroches, J., et al., 2000. Simulating fully 3D hydraulic fracturing. *Modeling in Geomechanics*, 525–557.
- CMG, 2003. *User's Guide STARS*. Computer Modelling Group Ltd, Calgary.
- Corey, A.T., 1954. The interrelation between gas and oil relative permeabilities. *Producers Monthly* 19 (1), 38–41.
- Deng, H., Dai, Z., et al., 2011. Simulation of CO<sub>2</sub> Sequestration at Rock Spring Uplift, Wyoming: Heterogeneity and Uncertainties in Storage Capacity, Injectivity and Leakage. Los Alamos National Laboratory (LANL).
- Dobrowol, J.E., 1999. An Extended Finite Element Method with Discontinuous Enrichment for Applied Mechanics. Northwestern University.
- Dusseault, M.B., Bilak, R., et al., 1996. Disposal of granular solid wastes in the western Canadian sedimentary basin by slurry fracture injection. In: Apps, J., Tsang, C.F. (Eds.), *Deep Injection of Hazardous Industrial Waste. Scientific and Engineering Aspects*, San Diego, CA, pp. 725–742.
- Fareo, A.G., Mason, D., 2011. A group invariant solution for a pre-existing fluid-driven fracture in permeable rock. *Nonlinear Analysis: Real World Applications* 12 (1), 767–779.
- Ferronato, M., Gambolati, G., et al., 2010. Geomechanical issues of anthropogenic CO<sub>2</sub> sequestration in exploited gas fields. *Energy Conversion and Management* 51 (10), 1918–1928.
- Fu, P., Johnson, S.M., et al., 2012. An explicitly coupled hydro-geomechanical model for simulating hydraulic fracturing in arbitrary discrete fracture networks. *International Journal for Numerical and Analytical Methods in Geomechanics*.
- Goerke, U.J., Park, C.H., et al., 2011. Numerical simulation of multiphase hydro-mechanical processes induced by CO<sub>2</sub> injection into deep saline aquifers. *Oil & Gas Science and Technology—Revue d'IFP Energies Nouvelles* 66 (1), 105–118.
- Haimson, B., Fairhurst, C., 1969. In-situ stress determination at great depth by means of hydraulic fracturing. In: *The 11th US Symposium on Rock Mechanics (USRMS)*, June 16–19, Berkeley, CA.
- Hillerborg, A., Modeer, M., et al., 1976. Analysis of crack formation and crack growth in concrete by means of fracture mechanics and finite elements. *Cement and Concrete Research* 6 (6), 773–781.
- Ji, L., Settari, A., et al., 2009. A novel hydraulic fracturing model fully coupled with geomechanics and reservoir simulation. *SPE Journal* 14 (3), 423–430.
- Kanninen, M.F., Popelar, C.H., 1985. *Advanced Fracture Mechanics*. Oxford University Press, New York.
- Knott, J.F., 1973. *Fundamentals of Fracture Mechanics*. Gruppo Italiano Frattura.
- Kovalyshen, Y., 2010. *Fluid-driven fracture in poroelastic medium*. Doctor, University of Minnesota (PhD thesis).
- Lecampion, B., 2009. An extended finite element method for hydraulic fracture problems. *Communications in Numerical Methods in Engineering* 25 (2), 121–133.
- Legarth, B., Huenges, E., et al., 2005. Hydraulic fracturing in a sedimentary geothermal reservoir: results and implications. *International Journal of Rock Mechanics and Mining Sciences* 42 (7–8), 1028–1041.
- Lucier, A., Zoback, M., Gupta, N., Ramakrishnan, T.S., 2006. Geomechanical aspects of CO<sub>2</sub> sequestration in a deep saline reservoir in the Ohio River Valley region. *Environmental Geosciences* 13 (2), 85–103.
- Mandl, G., Harkness, R., 1987. Hydrocarbon migration by hydraulic fracturing. *Geological Society, London, Special Publications* 29 (1), 39–53.
- Moës, N., Dolbow, J., et al., 1999. A finite element method for crack growth without remeshing. *International Journal for Numerical Methods in Engineering* 46, 131–150.
- Mohammadi, S., 2008. *Extended Finite Element Method for Fracture Analysis of Structure*. Blackwell Publishing Ltd., Oxford, UK.
- Morris, J.P., Detwiler, R.L., et al., 2011. The large-scale geomechanical and hydrogeological effects of multiple CO<sub>2</sub> injection sites on formation stability. *International Journal of Greenhouse Gas Control* 5 (1), 69–74.
- Murphy, H.D., Tester, J.W., et al., 1981. Energy extraction from fractured geothermal reservoirs in low-permeability crystalline rock. *Journal of Geophysical Research* 86 (B8), 7145–7158.
- Niels, S.O., Matti, R., 2005. *The Mechanics of Constitutive Modeling*. Elsevier, Amsterdam, The Netherlands.
- Olivella, S., Carrera, J., et al., 1994. Nonisothermal multiphase flow of brine and gas through saline media. *Transport in Porous Media* 15 (3), 271–293.
- Oliver, J., Huespe, A., et al., 2002. From continuum mechanics to fracture mechanics: the strong discontinuity approach. *Engineering Fracture Mechanics* 69 (2), 113–136.
- Osher, S., Sethian, J.A., 1988. Fronts propagating with curvature-dependent speed: algorithms based on Hamilton-Jacobi formulations. *Journal of Computational Physics* 79 (1), 12–49.
- Ouellet, A., Béard, T., et al., 2011. Reservoir geomechanics for assessing containment in CO<sub>2</sub> storage: a case study at Ketzin, Germany. *Energy Procedia* 4, 3298–3305.
- Pan, P.-Z., Rutqvist, J., et al., 2013. An approach for modeling rock discontinuous mechanical behavior under multiphase fluid flow conditions. *Rock Mechanics and Rock Engineering*, 1–15.
- Pan, P.-Z., Yan, F., et al., 2012. Modeling the cracking process of rocks from continuity to discontinuity using a cellular automaton. *Computers & Geosciences* 42 (0), 87–99.
- Pan, P.Z., Feng, X.T., et al., 2009. Coupled THM processes in EDZ of crystalline rocks using an elasto-plastic cellular automaton. *Environmental Geology* 57 (6), 1299–1311.
- Peirce, A., Detournay, E., 2008. An implicit level set method for modeling hydraulically driven fractures. *Computer Methods in Applied Mechanics and Engineering* 197 (33), 2858–2885.
- Peirce, A., Detournay, E., 2009. An Eulerian moving front algorithm with weak-form tip asymptotics for modeling hydraulically driven fractures. *Communications in Numerical Methods in Engineering* 25 (2), 185–200.
- Preisig, M., Prévost, J.H., 2011. Coupled multi-phase thermo-poromechanical effects. Case study: CO<sub>2</sub> injection at In Salah, Algeria. *International Journal of Greenhouse Gas Control* 5 (4), 1055–1064.
- Pruess, K., Moridis, G., et al., 1999. *TOUGH2 User's Guide, Version 2.0*. Lawrence Berkeley National Laboratory Berkeley, CA.
- Pruess, K., Spycher, N., 2007. ECO2N-A fluid property module for the TOUGH2 code for studies of CO<sub>2</sub> storage in saline aquifers. *Energy Conversion and Management* 48 (6), 1761–1767.
- Rashid, M., 1998. The arbitrary local mesh replacement method: an alternative to remeshing for crack propagation analysis. *Computer Methods in Applied Mechanics and Engineering* 154 (1–2), 133–150.
- Ren, Q., Dong, Y., et al., 2009. Numerical modeling of concrete hydraulic fracturing with extended finite element method. *Science in China Series E: Technological Sciences* 52 (3), 559–565.
- Richardson, C.L., Hegemann, J., et al., 2011. An XFEM method for modeling geometrically elaborate crack propagation in brittle materials. *International Journal for Numerical Methods in Engineering* 88 (10), 1042–1065.

- Rinaldi, A.P., Rutqvist, J., 2013. Modeling of deep fracture zone opening and transient ground surface uplift at KB-502 CO<sub>2</sub> injection well, In Salah, Algeria. *International Journal of Greenhouse Gas Control* 12 (0), 155–167.
- Rohmer, J., Seyed, D., 2010. Coupled large scale hydromechanical modelling for caprock failure risk assessment of CO<sub>2</sub> storage in deep saline aquifers.
- Rutqvist, J., 2011. Status of the TOUGH-FLAC simulator and recent applications related to coupled fluid flow and crustal deformations. *Computers & Geosciences* 37 (6), 739–750.
- Rutqvist, J., 2012. The geomechanics of CO<sub>2</sub> storage in deep sedimentary formations. *Geotechnical and Geological Engineering* 30 (3), 525–551.
- Rutqvist, J., Birkholzer, J., et al., 2007. Estimating maximum sustainable injection pressure during geological sequestration of CO<sub>2</sub> using coupled fluid flow and geomechanical fault-slip analysis. *Energy Conversion and Management* 48 (6), 1798–1807.
- Rutqvist, J., Birkholzer, J., et al., 2008. Coupled reservoir-geomechanical analysis of the potential for tensile and shear failure associated with CO<sub>2</sub> injection in multi-layered reservoir-caprock systems. *International Journal of Rock Mechanics and Mining Sciences* 45 (2), 132–143.
- Rutqvist, J., Stephansson, O., 2003. The role of hydromechanical coupling in fractured rock engineering. *Hydrogeology Journal* 11 (1), 7–40.
- Rutqvist, J., Tsang, C.F., 2002. A study of caprock hydromechanical changes associated with CO<sub>2</sub>-injection into a brine formation. *Environmental Geology* 42 (2), 296–305.
- Rutqvist, J., Vasco, D.W., et al., 2010. Coupled reservoir-geomechanical analysis of CO<sub>2</sub> injection and ground deformations at In Salah, Algeria. *International Journal of Greenhouse Gas Control* 4 (2), 225–230.
- Rutqvist, J., Wu, Y.S., et al., 2002. A modeling approach for analysis of coupled multiphase fluid flow, heat transfer, and deformation in fractured porous rock. *International Journal of Rock Mechanics and Mining Sciences* 39 (4), 429–442.
- Sarris, E., Papanastasiou, P., 2011. The influence of the cohesive process zone in hydraulic fracturing modelling. *International Journal of Fracture* 167 (1), 33–45.
- Segura, J.M., Carol, I., 2010. Numerical modelling of pressurized fracture evolution in concrete using zero-thickness interface elements. *Engineering Fracture Mechanics* 77 (9), 1386–1399.
- Shaffer, R., Thorpe, R., et al., 1984. Numerical and physical studies of fluid-driven fracture propagation in jointed rock.
- Shin, H., Santamarina, J.C., 2010. Fluid-driven fractures in uncemented sediments: underlying particle-level processes. *Earth and Planetary Science Letters* 299 (1), 180–189.
- Sih, G.C., Fracture, L.U.I.o., et al., 1973. *Handbook of Stress-intensity Factors*. Institute of Fracture and Solid Mechanics, Lehigh University.
- Sneddon, I.N., Elliot, H.A., 1946. The opening of a Griffith crack under internal pressure. *Quarterly of Applied Mathematics* (4), 262–267.
- Tran, D., Nghiem, L., et al., 2010. Study of geomechanical effects in deep aquifer CO<sub>2</sub> storage. In: *44th US Rock Mechanics Symposium and 5th US-Canada Rock Mechanics Symposium*.
- USEPA, 1994. Determination of Maximum Injection Pressure for Class I Wells. In: *US Environmental Protection Agency region 5—Underground Injection Control Section Regional Guidance # 7*. EPA, Washington, DC.
- van Genuchten, M.T., 1980. A closed-form equation for predicting the hydraulic conductivity of unsaturated soils. *Soil Science Society of America Journal* 44 (5), 892–898.
- Villarrasa, V., Bolster, D., et al., 2010. Coupled hydromechanical modeling of CO<sub>2</sub> sequestration in deep saline aquifers. *International Journal of Greenhouse Gas Control* 4 (6), 910–919.
- Wang, J.J., Zhu, J.G., et al., 2007. Experimental study on fracture toughness and tensile strength of a clay. *Engineering Geology* 94 (1), 65–75.
- Wang, W., Kolditz, O., 2007. Object-oriented finite element analysis of thermo-hydro-mechanical (THM) problems in porous media. *International Journal for Numerical Methods in Engineering* 69 (1), 162–201.
- Xu, B., Wong, R., 2010. A 3D finite element model for history matching hydraulic fracturing in unconsolidated sands formation. *Journal of Canadian Petroleum Technology* 49 (4), 58–66.
- Zang, A., Stephansson, O., 2008. *Stress Field of the Earth's Crust*. Springer, London, UK.
- Zhang, X., Jeffrey, R., et al., 2011. Initiation and growth of a hydraulic fracture from a circular wellbore. *International Journal of Rock Mechanics and Mining Sciences* 48 (6), 984–995.
- Zhang, Z.X., 2002. An empirical relation between mode I fracture toughness and the tensile strength of rock. *International Journal of Rock Mechanics and Mining Sciences* 39 (3), 401–406.
- Zoback, M.D., 2007. *Reservoir Geomechanics: Earth Stress and Rock Mechanics Applied to Exploration, Production and Wellbore Stability*. Cambridge Press.